LUNDS UNIVERSITET

Numerical Investigations of a Partitioned FSI Algorithm for Tetra Pak's Filling Tube

Leo Andersson

Thesis for the degree of Master of Science in Engineering
Division of Fluid Mechanics
Department of Energy Sciences
Faculty of Engineering | Lund University

Numerical Investigations of a Partitioned FSI Algorithm for Tetra Pak's Filling Tube

Leo Andersson

June 2016, Lund

This degree project for the degree of Master of Science in Engineering has been conducted at the Division of Fluid Mechanics, Department of Energy Sciences, Faculty of Engineering, Lund University, and at Tetra Pak, Lund

Supervisor at the Division of Fluid Mechanics was Professor Johan Revstedt
Supervisors at Tetra Pak were Michael Olsson, Ulf Engdar, Anders Magnusson
Examiner at Lund University was Professor Christoffer Norberg

The project was carried out in cooperation with Tetra Pak

Thesis for the Degree of Master of Science in Engineering

ISRN LUTMDN/TMHP-16/5368-SE

ISSN 0282-1990

Fluid Mechanics
Department of Energy Sciences
Faculty of Engineering, Lund University
Box 118, 221 00 Lund
Sweden

www.energy.lth.se

Abstract

Numerical simulations of fluid-structure interaction of a water-filled tube with a free surface are conducted using an implicit partitioned coupling scheme. Abaqus and STAR-CCM+ are used for the solid- and fluid domains respectively. This application has stability issues, with the most severe turning out to be the added mass effect. Rayleigh β damping and grid flux under-relaxation has been used to keep simulations stable and these parameters' effect on the solution and stability are investigated. A model problem consisting of a completely filled tube of a linear elastic material and a potential flow is analysed with respect to stability, considering the HHT time integration scheme used in Abaqus. A criterion for the displacement under-relaxation factor ω is found, depending on the geometry, material parameters, β and time step. The impact on stability of changing these parameters is discussed and the stability criterion is validated against simulations. An effort is made to provide suitable settings and recommendations for future simulations.

It is found that β damping is very effective in stabilising the algorithm, but changes the solution significantly. Grid flux under-relaxation also helps stabilise the solution, but the mechanism is not clear and its effect on the solution is erratic. It turns out that smaller time steps have a destabilising effect on the partitioned algorithm, and so do long tubes, thin, weak structures and heavy fluids. The added mass effect can be mitigated by lowering ω, but at the cost of computation time. The results of numerical experiments are in good agreement with the criterion established by the model problem. Some additional factors influencing stability are discussed, including viscosity, the effect of an obstructed flow, boundary conditions, a nonlinear finite element formulation and a higher order time discretisation scheme.

Keywords: fluid-structure interaction, FSI, added mass effect, partitioned implicit scheme, stability, Rayleigh damping, grid flux under-relaxation

Acknowledgements

I would like to thank my thesis advisors for the opportunity to do this interesting project and their support during the process. Michael Olsson, Ulf Engdar and Anders Magnusson at Tetra Pak for the advice, experience and practical help they provided in doing the numerical investigations for this thesis, and their valuable input during the writing process. In particular Michael Olsson for the frequent discussions where many interesting results were found and his help in structuring the work. Also Johan Revstedt at the Division of Fluid Mechanics, Lund University for his comments and advice during the process as well as the administrative tasks.

Contents

Chapter 1

Introduction

Tetra Pak is one of the world's largest developers of food packaging technology, and as such simulations of processes and products are essential to ensure a safe and reliable production. This thesis concerns numerical investigations of the filling tube application, as shown in figure 1.1.

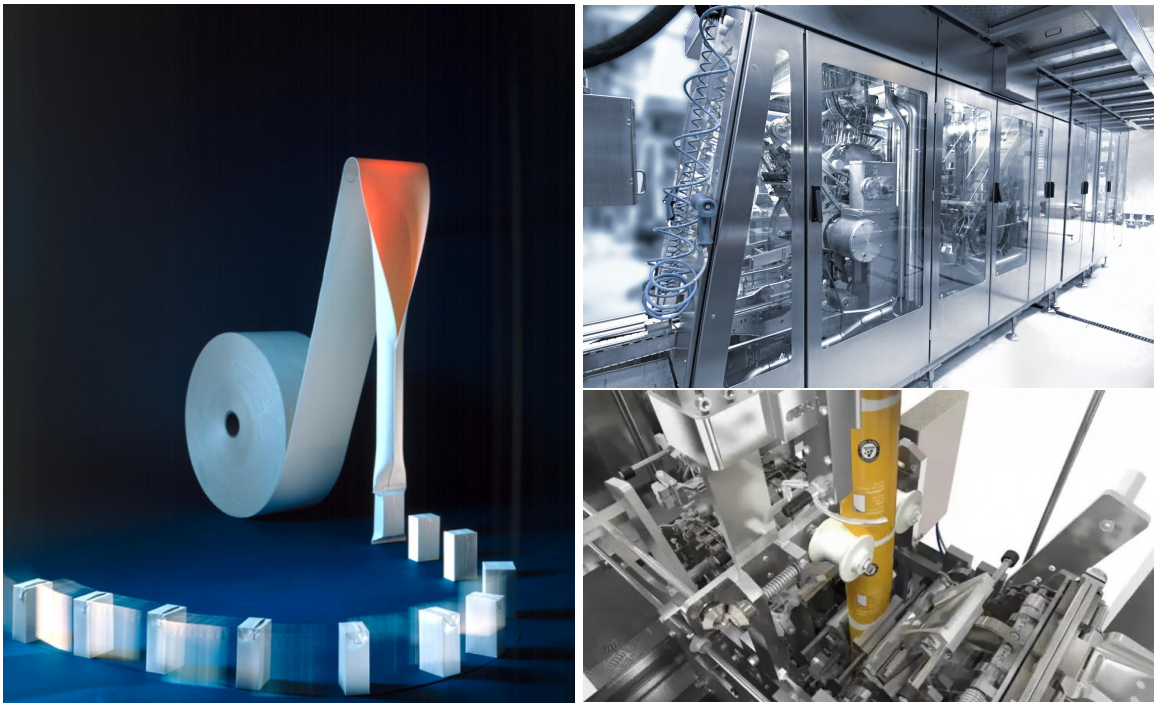

Figure 1.1: Visualisations of the filling tube, including the filling machine itself. Pictures courtesy of Tetra Pak.

In the filling machine a tube is formed by joining a paper-like sheet with a seam. Packages are then created by clamping and joining the tube below the fluid surface, sealing the liquid product inside. The fill pipe is located inside the tube and is connected to a floater device measuring the fluid level. This sealing process happens with a frequency of several packages per second, which gives rise to complex phenomena stemming from the interaction between the thin paper walls and the heavy fluid.

Frequently packaged fluids include milk, juice, yogurt, chocolate milk and many others. These fluids differ in viscosity and density and some even behave in a non-Newtonian manner, for example chocolate milk which may be described as a power-law fluid. There are also different packaging materials, sizes and filling speeds depending on the product and application.

1.1 Objective

In order to simulate the filling process Tetra Pak has developed computer models of the procedure, but there are uncertainties concerning the numerics. The simulations are subject to stability issues, and to counter these problems damping and grid flux under-relaxation has been employed. The question is if this significantly affects the solution and if there are better ways to keep the simulations stable. Therefore a geometrically simplified model of the tube has been implemented in order to save computational time and focus on the basic numerical properties. This simplified model is used to analyse the problem and to gain insight about the numerical issues affecting the original simulation.

The objective of this thesis is to investigate the effect of numerical parameters and schemes on the solution and stability. An effort is made to provide recommendations for future simulations on the full application in light of the obtained results.

Chapter 2

Fluid-Structure Interaction

Problems concerning fluids interacting with solids can be found practically everywhere in nature, for example the deflection of an air plane wing during flight or the bobbing motion of a boat. Therefore they are an interesting object of study, but are generally difficult to handle analytically and, it turns out, numerically as well.

Fluid-structure interaction is an example of a *coupled system*, a more general setting where two physical systems interact with each other and neither one can be solved without solving the other. A general definition of such problems has been provided by [1]

Coupled systems and formulations are those applicable to multiple domains and dependent variables which usually (but not always) describe different physical phenomena and in which
(a) neither domain can be solved while separated from the other;
(b) neither set of dependent variables can be explicitly eliminated at the differential equation level.

2.1 The Harmonic Oscillator

In order to introduce the concept of fluid-structure interaction (FSI), consider the single degree-of-freedom system in figure 2.1. A sphere of mass m is suspended on a spring of stiffness k, moving in the z direction only. It is immersed in a fluid of density ρ_f under the assumption of inviscid, incompressible, rotation-free flow. The equations of motion can be written

$$m\ddot{z} + kz = f \tag{2.1}$$

where f is an external force on the sphere. According to potential flow theory a sphere with acceleration $\ddot{z}$ will accelerate some amount of fluid mass m_a, and by Newton's laws this will cause a reaction force on the body. Therefore equation 2.1 can be written

$$m\ddot{z} + kz = -m_a\ddot{z} \Leftrightarrow (m + m_a)\ddot{z} + kz = 0. \tag{2.2}$$

This is the equation for a harmonic oscillator with characteristic frequency $\sqrt{\frac{k}{m+m_a}}$. It can be shown that the added mass for a sphere $m_a = \frac{2}{3}\rho_f \pi r^3$.

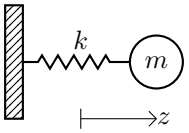

Figure 2.1: A mass suspended on a spring, free to move in the z direction

In reality fluids are often viscous, and one could imagine a viscous reaction force $f = -c_a \dot{z}$ acting on the sphere, dissipating energy as it oscillates. There are even situations where an added stiffness $f = -k_a z$ could be considered, for example when a displacement changes hydrostatic pressure by moving the level of a free surface.

For an arbitrary geometry the added mass is different depending on the direction of acceleration, and has to be described by an added mass tensor m_{ij} describing the forces and moments caused by an acceleration. [2]

For a more complex system, for example a system of equations obtained by the finite element method, the added mass is described by a matrix. In this case the equations of motion in (2.2) would take the form

$$\mathbf{M}\ddot{\mathbf{d}} + \mathbf{K}\mathbf{d} = -\mathcal{M}_A \ddot{\mathbf{d}}. \tag{2.3}$$

where $\mathcal{M}_A$ is the added mass matrix. The dynamical equations for the tube wall will take this form in the following analysis. The added mass matrix is generally not known in closed form, and therefore fluid dynamics simulations have to be performed to find the forces on the solid. In real life cases one is rarely interested in the simplified flow assumed above, so simulations are necessary anyway.

2.2 Numerical FSI

Numerical simulations of fluid-structure interaction can be done by either considering the coupled problem as one system of equations where the flow- and displacement fields are solved simultaneously, or by iteratively solving the solid- and fluid domain separately, transferring forces and displacements between the calculations. The former approach is called *monolithic* and the second *partitioned*. A monolithic treatment generally requires custom built software for highly specialised applications while partitioned simulations can be carried out using general-purpose fluid- and solid mechanics solvers, communicating via some protocol.

In the partitioned approach there are two main schemes: explicit and implicit. Common to these is that the solid equations are solved, then the displacements are imported into the fluid dynamics solver where a mesh morpher makes sure the mesh is still proper for the updated geometry, and a flow field is obtained. The explicit method then takes a time step while the implicit runs this inner loop until convergence, then takes a step.

Using a partitioned scheme the added mass effect can cause the algorithm to become unstable. This problem can be mitigated by under-relaxing the displacements imported into the fluid solver, but comes at the cost of slower convergence. [3]

Handling the added mass instability will turn out to be the main subject of this thesis, and some useful results regarding stability are established. There is a very interesting connection between the material parameters and geometry of the problem and the time step and displacement under-relaxation factor. Light, weak structures interacting with heavy fluids turns out to worsen the added mass instability, and so does smaller time steps. Thus, trying to make a partitioned FSI simulation stable by decreasing the time step would be counter-productive.

Chapter 3

Problem Definitions

The equations governing this problem are the solid mechanics relations for a linearly elastic material in the finite strain regime for the wall, and the Navier-Stokes equations in the fluid. These two domains are connected by an interface Σ, best thought of as the wet surface on the wall. The boundary conditions imposed by the FSI coupling are, in words: the fluid domain follows the motion of the walls and the stress tensor from the solid- and fluid- equations are in balance on Σ. A conceptual sketch of the information transfer over Σ is outlined in figure 3.1 where forces and displacements are exchanged between the domains. Here p and τ_w denote the pressure at the wall and wall shear stress respectively, which are imported as a stress tensor $\boldsymbol{\sigma}$ into the solid calculation, $\mathbf{d}$ is the displacement of the wall which together with its derivatives becomes the boundary conditions for the velocity field $\mathbf{u}$ in the fluid domain.

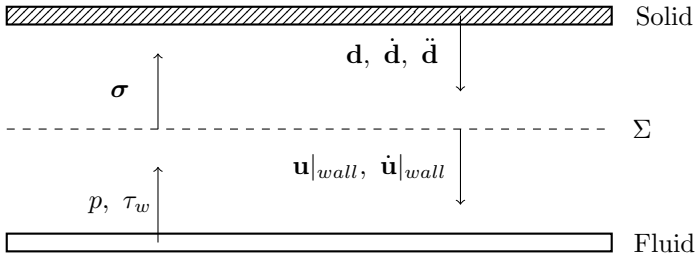

Figure 3.1: A sketch of the computational domains, including the interface Σ where exchange of information between the solid- and fluid domains occurs.

This problem is discretised by the finite element method for the wall and the finite volume method for the fluid, coupled via the implicit partitioned approach.

3.1 The Model

In order to reduce the complexity and to focus on the numerical aspects of the simulations a simplified model was created. It consists of two parts: the CFD mesh of the fluid domain and the FEM mesh of the tube wall. The tube is 0.753 m long and has a radius of 0.0267 m.

The model uses a fixed inlet pipe and floater and a continuous slit around the inlet pipe where there were separate holes in the original CAD model, with the same area. This is in order to reduce the number of cells needed while still hopefully capturing the relevant physical behaviour.

3.1.1 The CFD Model

Pictured in figure 3.2 is a plane cut of the mesh in the fluid domain and a 3D model of the tube slanted for perspective. The mesh is a trimmed 3D mesh with around 1.6 million cells, refined around the corners and the boundary layers.

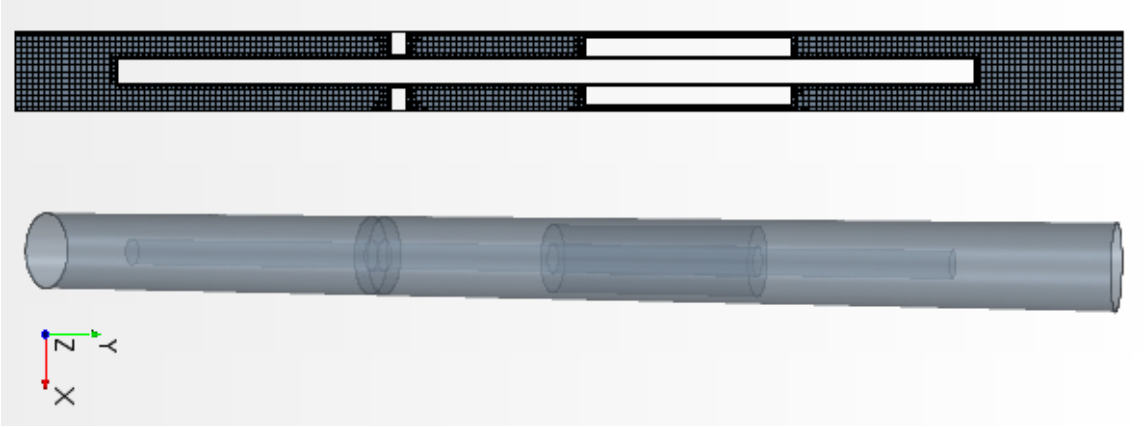

Figure 3.2: CFD mesh and 3D model. The outlet is to the left in this image, the fill pipe outlet is directed towards the outlet, the thin disk is the pressure flange, and the cylinder to the right is the floater.

The Navier-Stokes equations governing the flow are treated as URANS and discretised by the finite volume method, implemented in STAR-CCM+.

Boundary conditions are non-slip walls on all surfaces except the fill pipe inlet, and the upper and lower openings of the tube. On the lower boundary, here called *outlet*, the boundary condition is a mass flow inlet as implemented in STAR-CCM+ with a time dependent flow profile specified by an experimental measurement. The fill pipe inlet has a constant mass flow rate balancing the fluid level over a period. There is a free surface about half-way up the floater, and the two-phase physics is modelled by the Volume of Fluid (VOF) method, which is an Eulerian multiphase method suitable for relatively large free surfaces between non-mixing fluids. [4] The upper boundary is set as a pressure outlet for air with reference pressure 200 Pa. The tube wall moves in the negative y-direction with a constant speed of about 0.5 m/s, implemented by setting the fluid velocity at the wall to match this speed.

3.1.2 The FEM Model

On the solid side, an Abaqus case was set up using rectangular linear shell elements of size 2×2 mm. The tube wall has a thickness of one third of a millimetre, and there is a seam running along the length of the tube of double thickness, with a width chosen to be 5 mm. The boundary conditions make sure the tube is fixed around the perimeter at the bottom, and permitted to move only in the lengthwise y-direction at the top. There is also an applied load to account for the web tension applied by the machine stretching the tube lengthwise, applied uniformly to the upper perimeter.

The material is an orthotropic elastic material. Young's modulus in the axial direction is $E_{MD} = 5855$ MPa, in the tangential direction about half of this $E_{CD} \approx 0.5E_{MD}$, and the shear modulus between these was chosen as $G_{12} = 0.39\sqrt{E_{MD}E_{CD}}$ as a heuristic criterion. Thus the material parameters can be varied by changing E_{MD} and the rest will scale in an appropriate and physically correct manner.

3.1.2.1 Finite Element Formulation

The equations of motion for a solid body under large deformations in a Lagrangian setting can be written as

$$\frac{\partial P_{ij}}{\partial x_j} + \rho^0 b_i = \rho^0 a_i \tag{3.1}$$

where $\mathbf{P}$ is the first Piola-Kirchhof stress tensor, $\mathbf{b}$ the body forces, $\mathbf{a}$ the displacement field and ρ^0 the density, all in the reference configuration.

These equations can be discretised using the Galerkin method to yield the matrix equation

$$\mathbf{M}\ddot{\mathbf{d}} + \mathbf{C}\dot{\mathbf{d}} + \mathbf{F}_{int}(\mathbf{d}) = \mathbf{F}_{ext}(t) \tag{3.2}$$

Here $\mathbf{M}$ is the usual mass matrix, consisting of the form functions integrated over the reference configuration, $\mathbf{C}$ is a damping matrix, and $\mathbf{F}_{int}(\mathbf{d})$ is the inner force vector caused by the displacement vector $\mathbf{d}$. One can identify $\mathbf{F}_{int}(\mathbf{d}) = \mathbf{K}\mathbf{d}$ where $\mathbf{K}$ is the tangential stiffness matrix, i.e the linearisation of the inner forces around the current displacement configuration. [5]

3.1.3 FSI Coupling

We seek a solution to the dynamical equations describing the flow field and solid displacement field. These are physically coupled via the force exerted on the interface Σ by the fluid (pressure, wall shear stress), and moving walls changing the fluxes and boundary conditions of the flow. Recall figure 3.1.

The two models are linked via Simulia's co-simulation protocol allowing exchange of information between the FEM- and CFD calculations.

Denote the flow field $\mathbf{u}$, the wall displacement vector $\mathbf{d}$, the flow solver $\mathcal{F}$, the solid solver $\mathcal{S}$. The implicit solution scheme is described in algorithm 1.

Algorithm 1 Implicit FSI algorithm

$\mathbf{u}_0^0 \leftarrow \mathbf{u}_{init}$ ▷ Initialisation
$\mathbf{d}_0^0 \leftarrow \mathbf{d}_{init}$
$n \leftarrow 0$ ▷ Time step 0
while $n < n_{max}$ **do** ▷ Run until maximum time
  $k \leftarrow 0$
  while $\mathbf{u}$ or $\mathbf{d}$ not converged **do** ▷ Check convergence. Loop only once: explicit scheme
    $\tilde{\mathbf{d}}_n^{k+1} \leftarrow \mathcal{S}(\mathbf{u}_n^k)$
    $\tilde{\mathbf{u}}_n^{k+1} \leftarrow \mathcal{F}(\mathbf{d}_n^k)$
    $\mathbf{d}_n^{k+1} \leftarrow \omega\tilde{\mathbf{d}}_n^{k+1} + (1-\omega)\mathbf{d}_n^k$ ▷ Under-relax the displacement vector with $0 < \omega \leq 1$
    $\mathbf{u}_n^{k+1} \leftarrow \tilde{\mathbf{u}}_n^{k+1}$
    $k++$
  end while
  $\mathbf{u}_{n+1}^0 \leftarrow \tilde{\mathbf{u}}_n^k$ ▷ Take time step
  $\mathbf{d}_{n+1}^0 \leftarrow \tilde{\mathbf{d}}_n^k$
  $n++$
end while

The pressure on the walls is ramped up by a factor going from 0 to 1 during an initial period $0 \leq t \leq t_{ramp}$, and so is the web tension in the Abaqus simulation. All simulations in this thesis use a partitioned implicit coupling.

3.1.4 Mass Flow Profile

The bottom surface was modelled as a mass flow inlet with a flow profile adapted from experiments. This can be seen in figure 3.3.

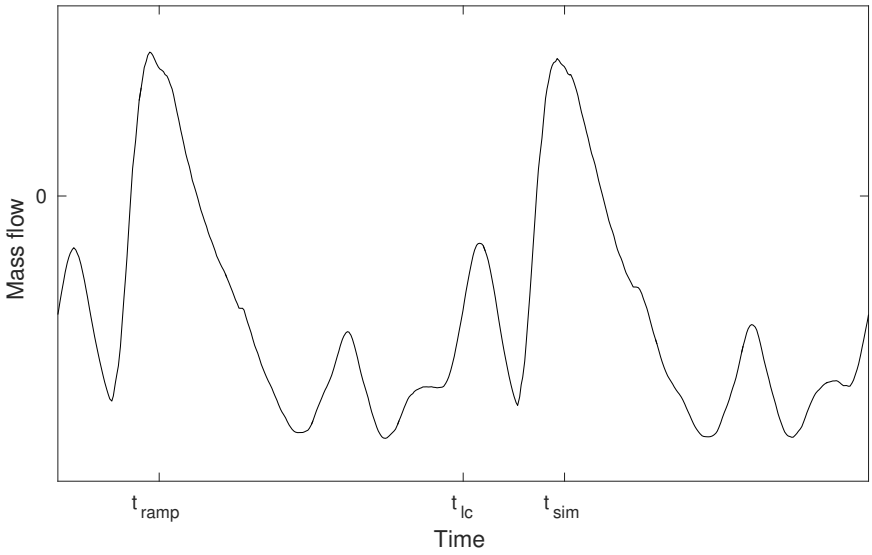

Figure 3.3: The mass flow profile imposed at the bottom outlet for two load cycles. Positive flow goes into the system, negative out.

Since some parameters are ramped up until t_{ramp} we will let each simulation run for the duration of one whole load cycle t_{lc} after this in order to study the unmodified behaviour for at least one cycle. Total simulation time is thus $t_{sim} = t_{lc} + t_{ramp}$.

3.1.5 Turbulence Modelling

The flow will pass several contractions and impingements. This may seem unsuitable for turbulent viscosity-based turbulence models, but experience indicates that this is not of critical importance. Since the most pressing problem is stability we have opted for a Realisable k-ε model as opposed to perhaps theoretically more suitable Reynolds Stress Models.

3.1.6 Compressible Fluid

The default liquid in these investigations is water, modelled as a compressible fluid with density $\rho_f = 1000 + \frac{p}{c^2}$ kg/m^3. The physical speed of sound in water is $c_{H_2O} \approx 1500$ m/s, but $c = 600$ m/s has been used for these calculations before at Tetra Pak for numerical reasons, so this will be used in the default case. The reasoning behind using a compressible equation of state for the liquid is to reduce the stiffness of the numerical problem, hopefully improving the stability. In cases where air bubbles are present in the liquid and flow in domains with flexible walls the actual speed of sound will decrease drastically, however these effects will not be considered in this thesis. [6][7]

3.1.7 Volume Of Fluid Two-Phase Model

The two-phase interaction is modelled with the VOF method. The two phases are slightly compressible water as defined above and compressible air, considered as an ideal gas. Experience indicates that the default parameters in STAR-CCM+ gives a too diffuse surface, so the lower- and upper Courant numbers were set high enough to stay in the HRIC scheme at all times: 500 and 1000 respectively. [4] This way the water/air surface will tend to stay sharper. The surface tension is constant 0.074 N/m with contact angles 76° for plastic on the fill pipe, flange and floater and 88° on the paper wall. Numerical damping was used to compensate for unphysical currents near the surface. This is

implemented as a numerical viscosity parameter which was set to the default value suggested by the software.

3.1.8 Integration Schemes

One has the option to choose the discretisation schemes in both Abaqus and STAR-CCM+.

Time integration in STAR-CCM+ is implemented as a first- or second order implicit scheme. [4]

$$\begin{cases} \dot{\mathbf{u}}^{n+1} = \frac{\mathbf{u}^{n+1}-\mathbf{u}^{n}}{\Delta t} & \text{1st order} \\ \dot{\mathbf{u}}^{n+1} = \frac{3\mathbf{u}^{n+1}-4\mathbf{u}^{n}+\mathbf{u}^{n-1}}{2\Delta t} & \text{2nd order} \end{cases} \tag{3.3}$$

The convection terms are handled by first- or second order upwind schemes. For gradient calculations we used exclusively the default second order Hybrid Gauss-LSQ method.

In Abaqus the time integration scheme was a second order Hilber-Hughes-Taylor (HHT) scheme with parameters corresponding to the *moderate dissipation* option. This is a generalisation of the Newmark scheme, adding a parameter α allowing for blending explicit and implicit terms. The scheme is defined by the following relations. [8]

$$\begin{cases} \mathbf{M}\ddot{\mathbf{d}}_{n+1} + (1-\alpha)\mathbf{C}\dot{\mathbf{d}}_{n+1} + \alpha\mathbf{C}\dot{\mathbf{d}}_{n} + (1-\alpha)\mathbf{K}\mathbf{d}_{n+1} + \alpha\mathbf{K}\mathbf{d}_{n} = (1-\alpha)\mathbf{F}_{n+1} + \alpha\mathbf{F}_{n} \\ \mathbf{d}_{n+1} = \mathbf{d}_{n} + \Delta t\dot{\mathbf{d}}_{n} + \Delta t^2((\frac{1}{2}-\upsilon)\ddot{\mathbf{d}}_{n} + \upsilon\ddot{\mathbf{d}}_{n+1}) \\ \dot{\mathbf{d}}_{n+1} = \dot{\mathbf{d}}_{n} + \Delta t((1-\gamma)\ddot{\mathbf{d}}_{n} + \gamma\ddot{\mathbf{d}}_{n+1}) \end{cases} \tag{3.4}$$

with $0 \leq \alpha \leq \frac{1}{2}$, $\gamma = \frac{1}{2} + \alpha$ and $\upsilon = \frac{1}{4}(1+\alpha)^2$. Thus the scheme is determined by α, which measures the amount of numerical damping. Moderate dissipation in Abaqus uses $\alpha = 0.41421$. Note that α has the opposite sign in Abaqus compared to the the notation used here, and we use υ instead of β in order to avoid confusion with the damping coefficient introduced later.

3.1.9 Grid Flux

With a dynamically moving mesh one has to account for the volume of fluid swept by the cell faces in each time step. This quantity is called the grid flux. STAR-CCM+ has numerical implementations to calculate this, and automatically chooses the scheme with the same discretisation order as the chosen time integration scheme. [4]

There is an option to set an under-relaxation factor on the grid flux which can help with convergence. However this means some of the displaced fluid will be ignored in the simulation, and some physical phenomena will be damped out and neglected or possibly amplified.

The convection term for the scalar transport equation at a face f is discretised as

$$[\phi\rho(\mathbf{v}\cdot\mathbf{a} - G)]_f = \phi_f\dot{m}_f \tag{3.5}$$

where $\dot{m}_f$ is the mass flux at the cell face, and ϕ_f is the scalar value, which is computed by a first- or second order upwind scheme. The general transport equation is handled equivalently.

The first order grid flux at a face is discretised as $G_f^n = \frac{\Delta V_f^n}{\Delta t}$ where ΔV_f^n is the volume swept by the surface over time step n. Applying an under-relaxation δ sets the grid flux to $G_f^n = \delta\frac{\Delta V_f^n}{\Delta t} + (1-\delta)G_f^{n-1}$.

3.1.10 Displacement Under-Relaxation Factor

When mapping the calculated nodal displacements $\tilde{d}$ into the fluid solver in the implicit FSI algorithm 1 one has the option to set an under-relaxation factor ω on the displacement vectors, thereby setting the displacements imported into the fluid solver to be $d^{k+1} = \omega\tilde{d}^{k+1} + (1-\omega)d^k$, where k is the index of the coupling step. This can help the algorithm converge but setting ω low may require more iterations to converge, slowing down the process.

3.1.11 Rayleigh Damping

The damping matrix $\mathbf{C}$ in equation 3.2 must be defined by the user according to the material properties or numerical requirements. A common method is to set $\mathbf{C} = \alpha\mathbf{M} + \beta\mathbf{K}$ for some $\alpha,\ \beta$. This is called Rayleigh damping, and these two parameters can be related to damping ratios of certain frequencies by the relation $\xi_n = \frac{1}{2\omega_n}\alpha + \frac{\omega_n}{2}\beta$. A damping ratio of 1 corresponds to critical damping of a certain frequency. [8] This relationship can be seen in figure 3.4.

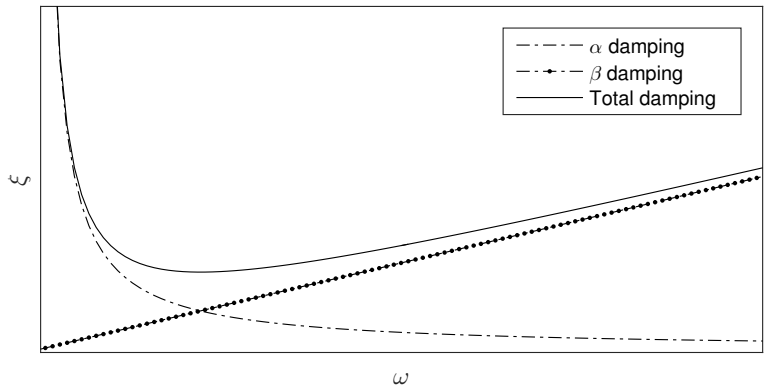

Figure 3.4: The relation between $\alpha,\ \beta$ and total damping.

Stiffness damping is used throughout this thesis, i.e $\alpha = 0$, since we would like to avoid damping out low frequencies corresponding to large slow movements of the tube wall. Note that this is not the same α as in the HHT scheme (3.4). Typically $\beta = 0.004$ has been used in these calculations at Tetra Pak, which causes critical damping at 80 Hz, see figure 3.5. This has been added to improve stability of the algorithm and is not motivated by theory or experiments. Most materials have some sort of damping, but it is not known if β damping is a suitable model for this cardboard material. Ideally one would like to remove this damping or at least decrease it to a level where it won't affect the solution significantly, and this will be one of the main topics for this thesis.

3.1.12 Contact Damping

Some simulations fail because the tube wall hits the pressure flange as a part of the dynamical procedure or possibly nonlinear, local numerical instabilities. This causes the mesh morpher to create cells with negative volume, and the fluid solver has to abort. In order to be able to get through these situations, a contact formulation can be made in Abaqus. We opted for *contact damping*, acting as a viscous force proportional to the wall velocity. A clearance distance c_0 and a damping parameter μ_0 are introduced, and the viscous force acting on the wall can be written $f = CAv$ where A is the nodal area, v the relative velocity between the wall and the flange and C a damping coefficient. The force starts to act on the wall c_0 length units away from the flange, and C is ramped up from 0 to μ_0 in that space. [8] c_0 was set as one fourth of the distance between the wall and the pressure flange.

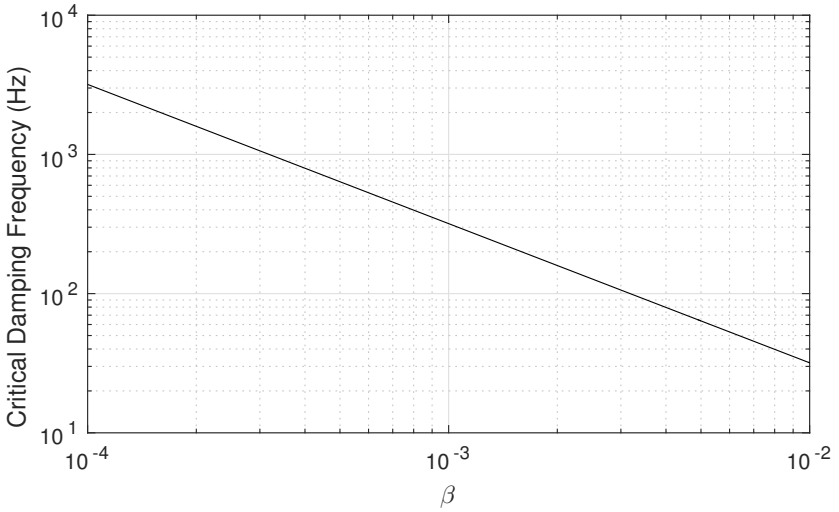

Figure 3.5: The critical damping frequency as a function of β.

3.1.13 Convergence Criteria

The residuals measure the solution's compliance to the Finite Volume equations, but in a complex real-world case like this it's hard to obtain very small residuals. If this is a problem of practical importance or not is hard to say, but in this case we have opted to measure convergence of the coupled FSI algorithm by asymptotic criteria on the total force acting on the wall and the incremental wall displacement. Each time step is considered converged if the total force on the tube wall $\int p \, \mathrm{d}A$ and the surface average of the incremental nodal displacement goes down to about one percent of the typical incrementation size for 15 iterations, using 4 inner iterations between each Abaqus calculation. These are heuristic criteria, but generally it seems to be a good compromise as the fluid residuals usually level off at the same time. For reference other asymptotic criteria have been explored: the lift coefficient on the bottom of the pressure flange and the surface integral of the magnitude of wall shear stress, but these exhibit similar behaviour, levelling off at the same time as the total force. One has to be careful as these types of integrated criteria do not guarantee convergence since one could have an infinite number of states with the same value of the integrated quantities on the wall. The Abaqus calculation has an internal convergence criterion, but the internal fluid convergence was not strictly monitored or accounted for, apart from the total wall pressure.

Chapter 4

Numerical Investigations

In this chapter some initial simulations are described, giving an intuition for the encountered problems. A method to investigate the identified critical parameters is defined. Then the general behaviour of simulations is discussed and some results are presented.

4.1 Initial Simulations

Both the FEM- and CFD cases were run standalone in order to check that the models were properly defined. Then some initial FSI calculations were made using single phase incompressible water and a constant inlet mass flow rate from the fill pipe, with a solid wall at the bottom and a pressure outlet at the top, with a time step of 5 ms and $\beta = 0.004$. This simple model behaved very well numerically and did not seem to be affected by any convergence problems. After this the model case described above was set up.

4.2 Convergence Issues

As a first candidate for a "best possible" parameter set, all time- and convection schemes were set to 2nd order, grid flux URF 1, nodal displacement URF 1, $\beta = 0$, incompressible water, and the various fluid under-relaxation factors to reasonable values that work for the static wall case. The time step was varied between 1-0.1 ms and the fluid URFs were tweaked, but all attempts failed to converge. Generally these cases became unstable during the first time step. It seems that some numerical compromises have to be made.

Next β was set to 0.004 while the time step was varied, but with no success.

Keeping these settings and introducing an adaptive displacement URF [0.2, 0.5] mitigated some problems, and the simulation was able to last a few time steps. However doing the same with $\beta = 0$ caused instabilities.

Even cases increasing β to 0.008, letting the displacement URF be 0.3 and setting the grid flux URF to 0.3 eventually became unstable after less than 0.02 s.

4.2.1 Base Case

Another case was defined using compressible water with sound of speed c=600 m/s, 1st order time integration, grid flux URF 0.7, $\beta = 0.004$, displacement URF 0.3, $\Delta t = 0.5$ ms and all convection schemes 2nd order. This managed to run for the whole period of 0.5 s, which we will interpret as fully convergent, and this became the **base case** for further investigations. The settings are summarised in table 4.1.

Time discretisation order	1
Convection discretisation order	2
Δt	0.5 ms
β	0.004
Displacement URF	0.3
Grid flux URF	0.7
Speed of sound	600 m/s

Table 4.1: The settings for the base case

Running the base case with $\beta = 0$ crashed, and all attempts to make it converge by decreasing the displacement URF, filtering the mass flow profile, using a linear geometry in Abaqus and trying c=200 and 1400 m/s failed.

This indicates that β is very important to the stability of the FSI coupling algorithm which brings up some important questions: why does it become unstable, how does β affect the solution and how low can we set β while maintaining convergence?

4.3 Investigative Method

In order to investigate the effect of a certain parameter, simulations were run starting from the base case, varying the parameter in question. The STAR-CCM+ case has a number of probes and measurements used for evaluating the results. The most important ones are the maximum overall wall displacement and the displacements of the probe points shown in figure 4.1.

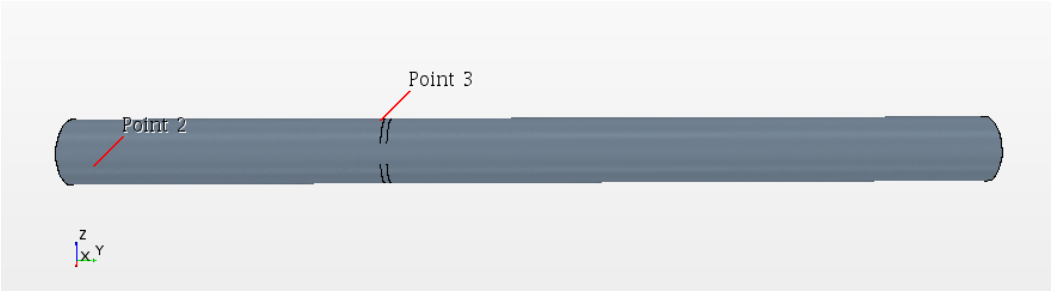

Figure 4.1: The locations of probe 2 and 3 on the tube wall.

4.4 General Behaviour

In a load cycle there are three main events happening, illustrated in figure 4.2.

- Tube Hit

  Fluid is pushed into the system with a peak at t_{ramp}. This causes high pressure under the pressure flange and bulging walls.

- Suction

  Fluid is pushed out rapidly through the tube at two occasions, noted suction 1 and 2. This causes the walls to contract and generally deform significantly.

Looking at a cross-section of the tube at the pressure flange one can identify a sinusoidal deformation with three peaks of the cross-section during suction. See picture 4.3 where the displacements are illustrated by a heavily magnified *vector warp*.

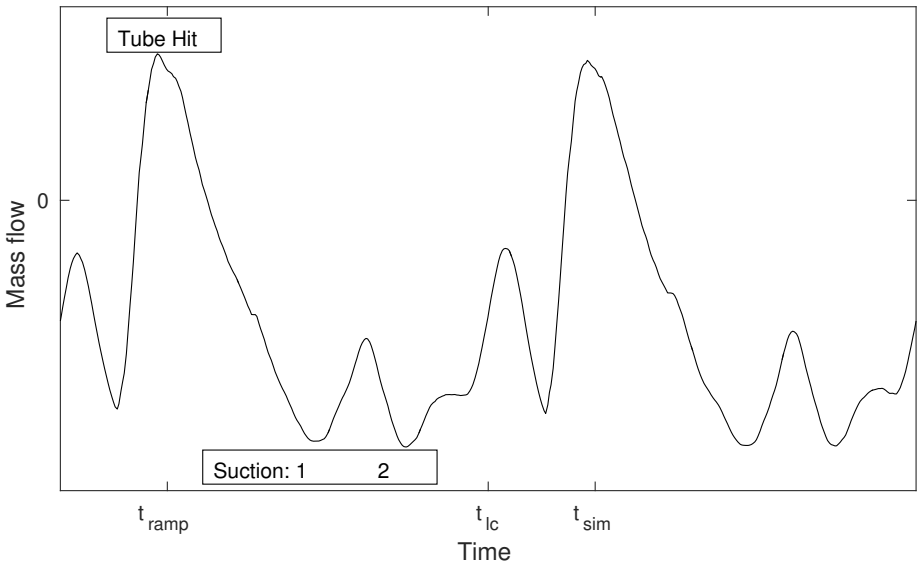

Figure 4.2: A simulation period with main events marked.

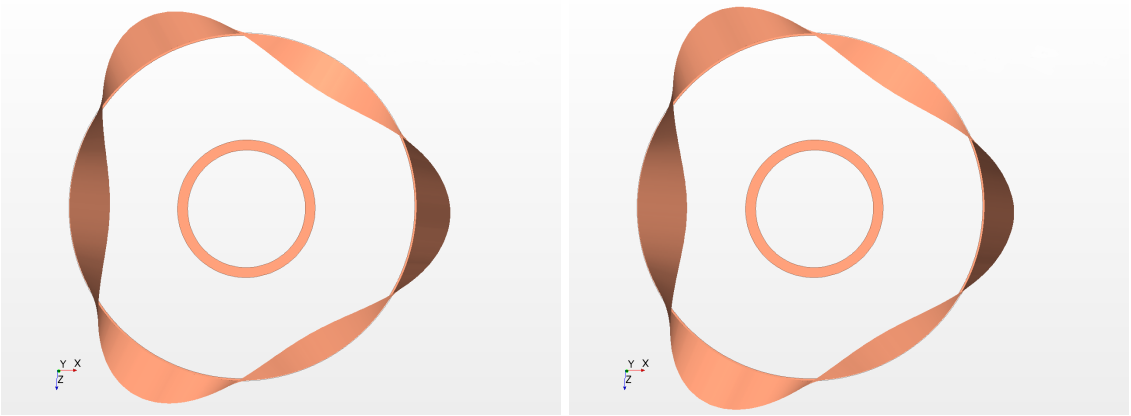

Figure 4.3: Cross-sections at the pressure flange during suction 1 and 2 respectively. The deformation profiles are very similar in shape and orientation.

During the tube hit the tube simply expands due to high pressure, primarily under the pressure flange. See figure 4.4. The seam of double thickness is located to the right which may explain the low displacements there.

The pressure around the pressure flange seems to have a sinusoidal behaviour in the tangential direction. Take for example two instantaneous images, seen in figure 4.5, plotted as a function of $0 \leq \theta \leq 2\pi$ where $\theta = 0$ corresponds to the position of the seam on the tube. The most common shape by far is the one with four peaks, seen in the first image. However at times one can also see different shapes, like the one with three peaks shown in the second image in figure 4.5.

Figure 4.4: Cross-section at the pressure flange during the tube hit.

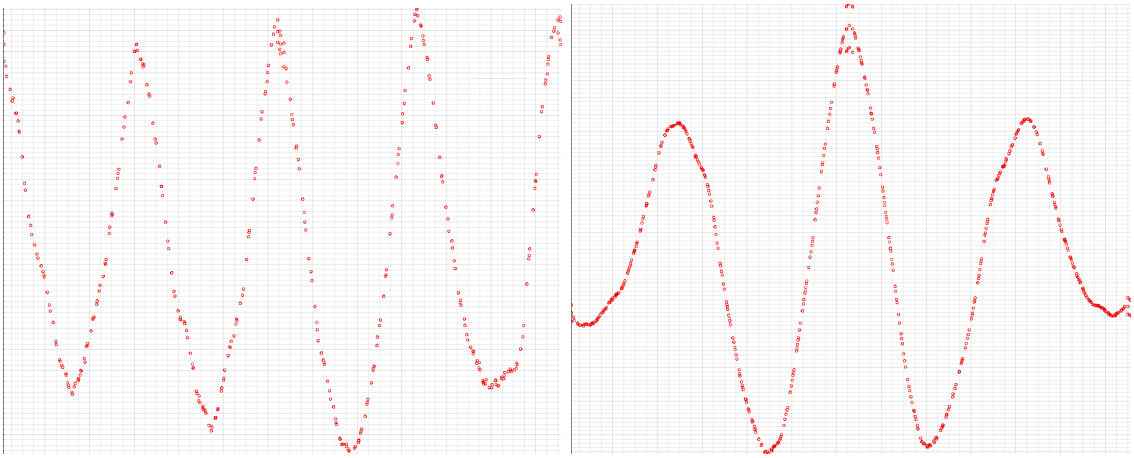

Figure 4.5: Pressure profiles at the flange at different times. Vertical axis denotes pressure, which is removed due to confidentiality. Horizontal is the tangential coordinate $0 \leq \theta \leq 2\pi$.

4.5 β Damping

Several simulations were made in order to investigate the effect of β on the solution. Using the base case as a reference, β was set to 0.001, 0.003, 0.004 and 0.01, and the results can be seen in figures 4.6-4.8, where the total displacement of each probe is plotted. Note that the simulation with $\beta = 0.001$ crashed into the wall at suction 1 and $\beta = 0.003$ at suction 2. One can see that increasing β has a damping effect on the solution, and especially with $\beta = 0.01$ the peaks at suction 1 and 2 are almost completely damped out, but not the tube hit.

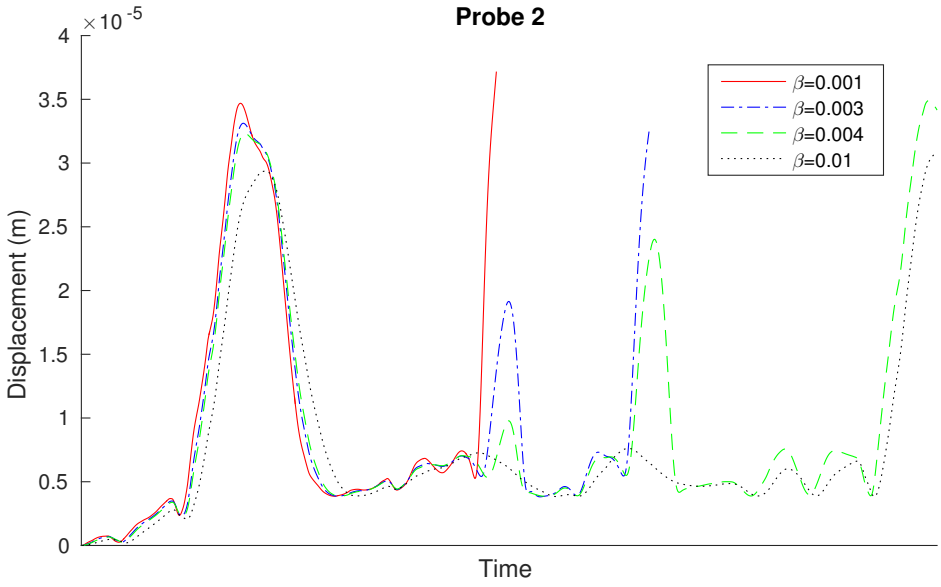

Figure 4.6: The solutions for varying β measured at probe 2.

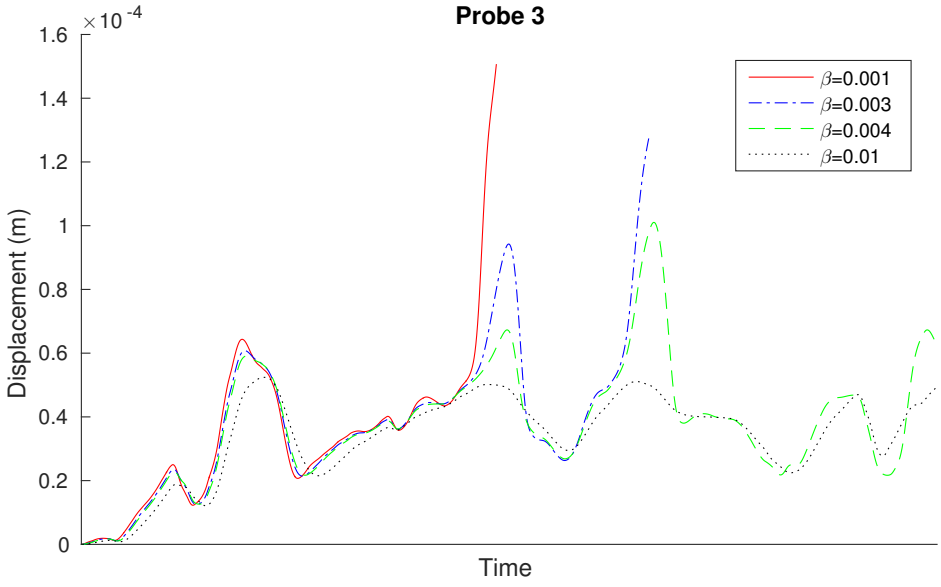

Figure 4.7: The solutions for varying β measured at probe 3.

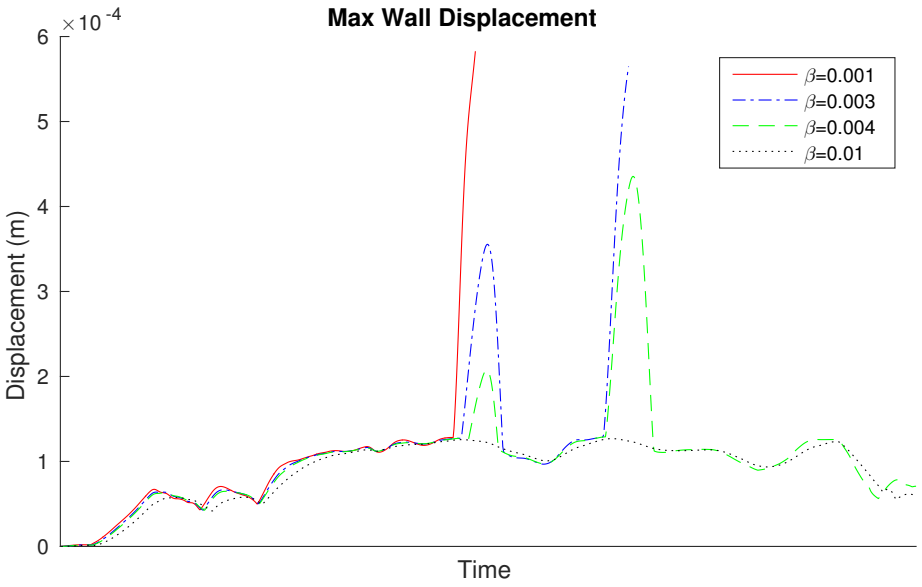

Figure 4.8: The solutions for varying β, maximum wall displacement.

4.6 Grid Flux

The grid flux was set to 0.3, 0.7 and 1 for the base case using first order time integration. The solutions are available in figures 4.9-4.11. The maximum wall displacement is effectively unaffected, but especially probe 3 shows a large difference. Surprisingly using both grid flux URF 0.3 and 1 there appears an extra peak towards the end in probe 3 (figure 4.10), which is not present or at least heavily damped out with grid flux URF 0.7. The magnitude of these peaks does not follow any order, with the largest for grid flux URF 1, the smallest for 0.7 and 0.3 in between.

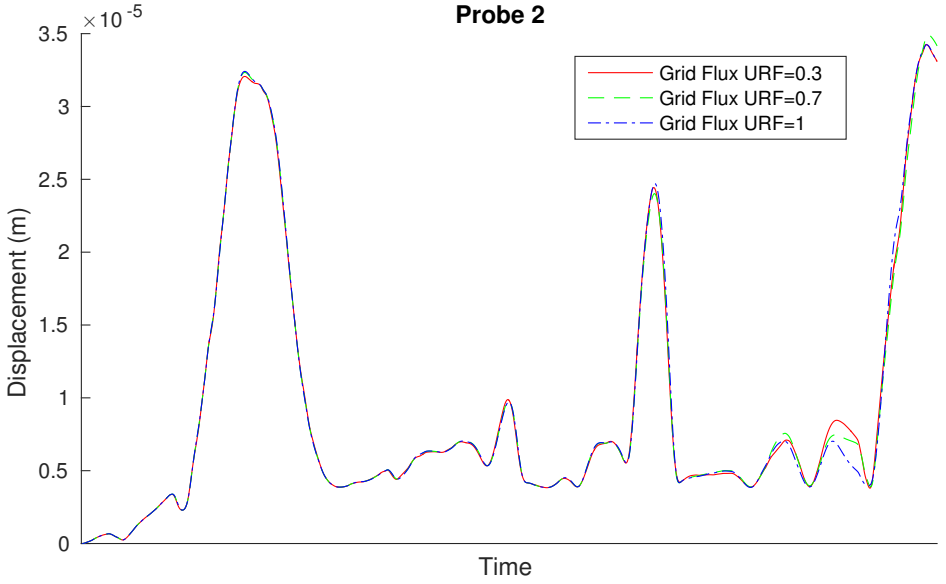

Figure 4.9: The solutions for varying grid flux under-relaxation measured at probe 2.

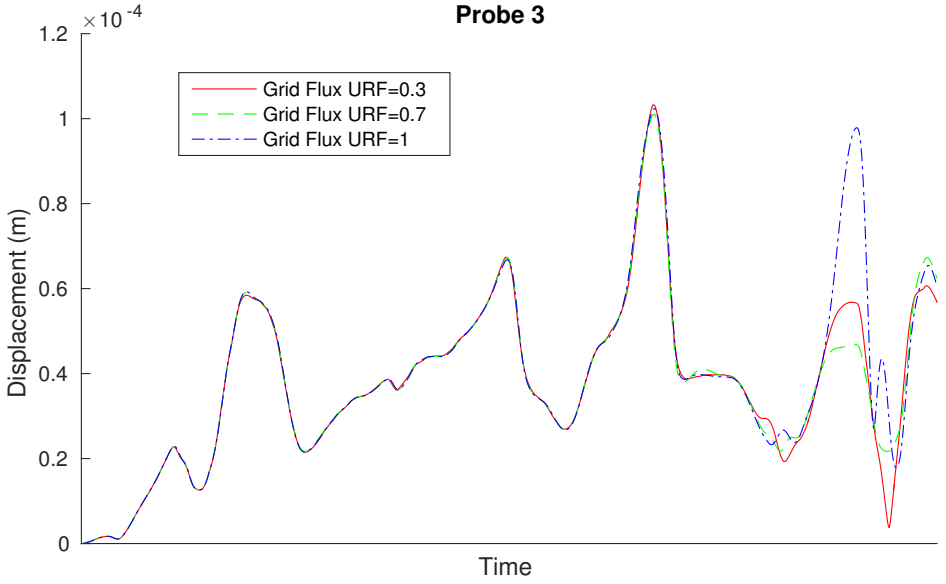

Figure 4.10: The solutions for varying grid flux under-relaxation measured at probe 3.

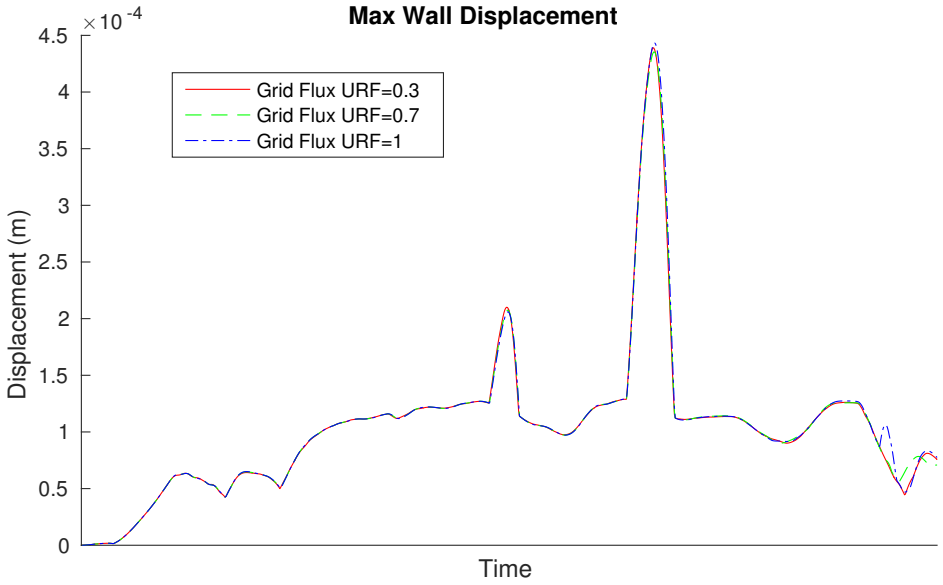

Figure 4.11: The solutions for varying grid flux under-relaxation, maximum wall displacement.

4.7 Time Discretisation Order

The time discretisation was set to second order, run with $\beta = 0.004$, using grid flux under-relaxation 0.7 and 1 respectively, and compared to the base case. Solutions are available in figures 4.12-4.14. These solution histories don't seem to differ very much, except for a small difference at the end of figure 4.14.

The second order time integration does have an effect on the displacement which may be underestimated from the first three figures. The radial displacement in probe 3 can be seen in figure 4.15, when using grid flux 1. One can see large differences in displacement and behaviour between the first- and second order time integration schemes. It can be noted that the 1st order time integration seems to have larger displacements than the second order towards the end, which may be surprising since first order methods are generally more dissipative.

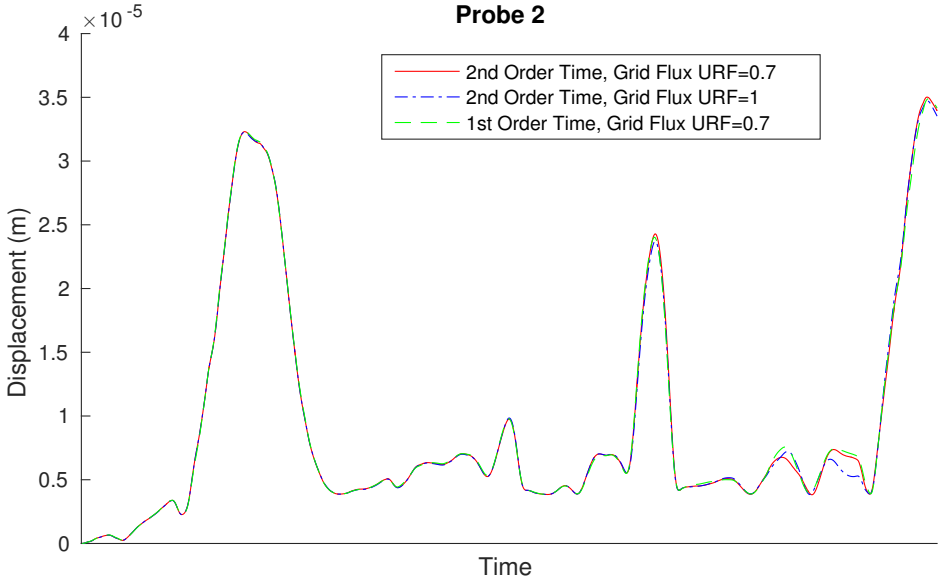

Figure 4.12: The solutions for varying time discretisation order measured at probe 2.

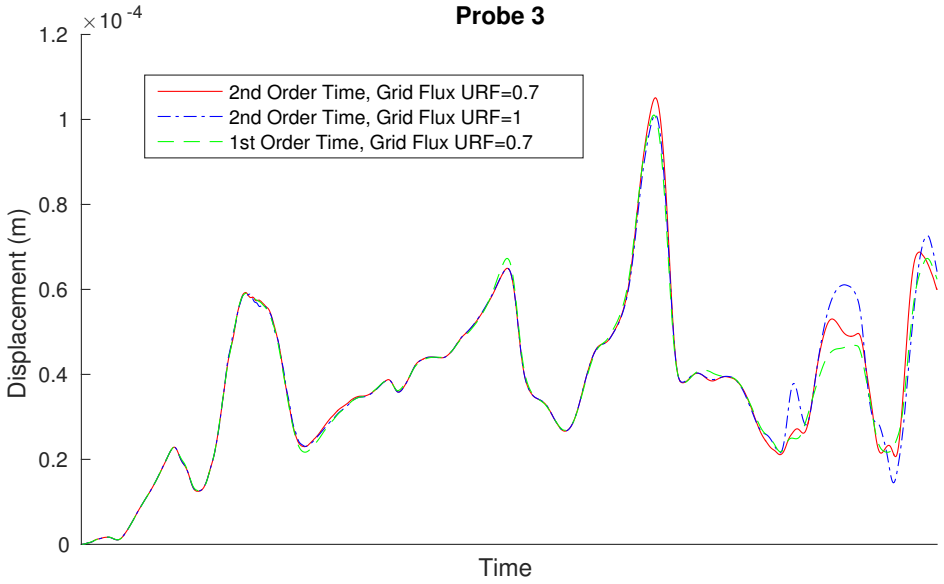

Figure 4.13: The solutions for varying time discretisation order measured at probe 3.

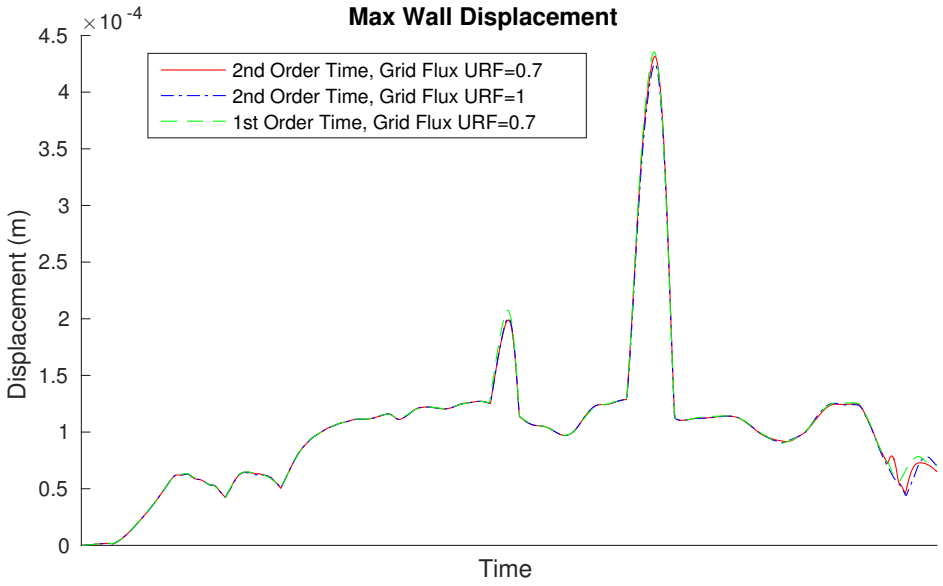

Figure 4.14: The solutions for varying time discretisation order, maximum wall displacement.

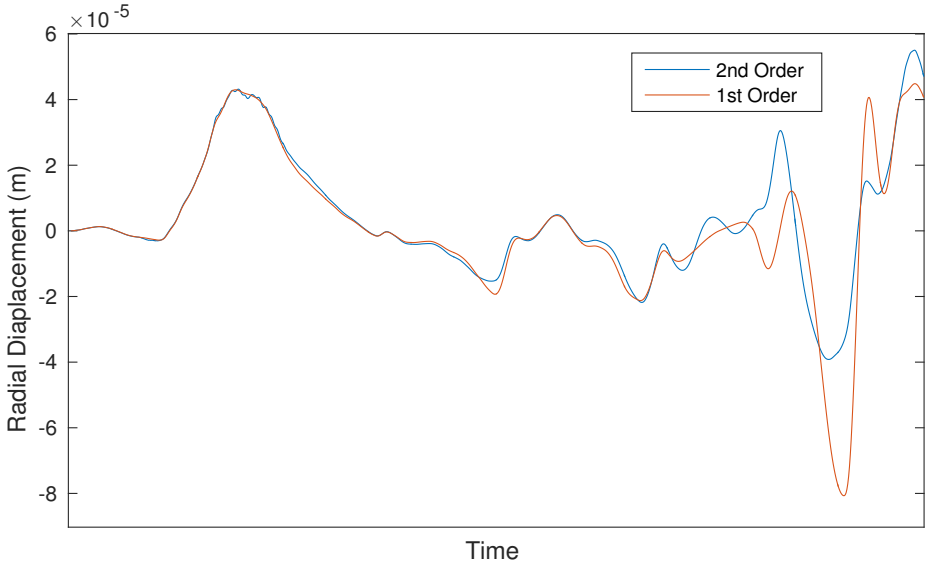

Figure 4.15: The radial displacement in probe 3 using 1st and 2nd order time integration and grid flux 1.

Chapter 5

Stability Analysis

It has been known for some time that the added mass effect causes stability issues in partitioned FSI simulations. Experience indicates that long tubes, weak structures and heavy fluids cause trouble numerically, and to estimate the effect of these parameters some model problems can be considered. In this section we will study some simplified problems using certain time integration schemes to better understand the causes of the added mass instability, and to predict the onset of numerical difficulties.

5.1 A 2D Model

In order to investigate these effects Causin et al. studied the numerical stability of a simplified 2D model of a blood vessel. [9] A sketch of the geometry can be seen in figure 5.1. The displacements on the wall are radially symmetric and the governing equations for the radial displacement along the length axis are

$$\begin{cases} \rho_s h_s \ddot{\eta} + a\eta - b\frac{\partial^2 \eta}{\partial x^2} = f & \text{on } \Omega_S \ \forall t \in [0,T] \\ \eta = 0 & \text{on } \partial\Omega_f \ \forall t \in [0,T] \end{cases} \tag{5.1}$$

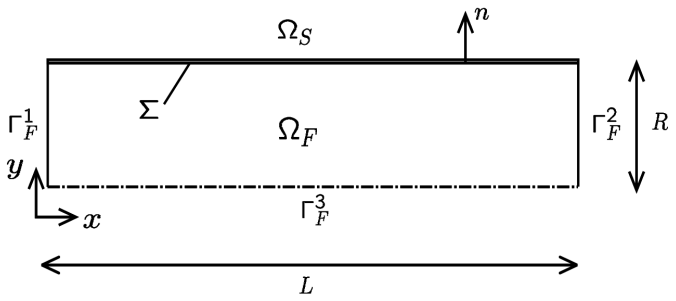

Figure 5.1: The simplified geometry of the 2D model problem with symmetry axis.

Here h_s is the wall thickness, ρ_s the solid's density, $a = Eh_s/[r^2(1-\nu^2)]$ for Young's modulus E, radius r and Poisson's ratio ν, $b = \kappa_T G h_s$, κ_T being the Timoshenko shear correction factor and G the shear stress modulus. This two-dimensional "tube" is filled with a fluid of density ρ_f under potential flow in the fluid domain Ω_f. Thus the added mass effect can be written $f = -\mathcal{M}_A \ddot{\eta}$, where $\mathcal{M}_A$ is the added mass operator, i.e the continuous counterpart of the added mass matrix. The authors of [9] analyse some time integration schemes, letting $b = 0$ in equation 5.1. The maximal eigenvalue of the added mass matrix turns out to be important, and is denoted $\rho_f \mu_{max}$.

5.1.1 Explicit Scheme

Consider using a first order implicit Euler scheme for the fluid velocities and a leap-frog scheme for the structure, advancing in an explicit manner in time. It turns out that this scheme is *unconditionally unstable* for

$$\frac{\rho_s h_s}{\rho_f \mu_{max}} < 1. \tag{5.2}$$

This means that if the structure has thin walls, is light compared to the fluid or has a large added mass effect this scheme will not converge for any choice of time step.

In [10] it is shown that for every explicit coupling scheme where the fluid- and solid solvers work implicitly internally, there is a criterion $\frac{\rho_s h_s}{\rho_f \mu_{max}} < C$ for some C depending on the scheme.

5.1.2 Implicit Scheme

Now consider a first-order backwards difference scheme for both the structure and the fluid solver, using the partitioned implicit FSI algorithm. The following stability criterion for the displacement under-relaxation ω was found (5.3)

$$0 < \omega < \frac{2(\rho_s h_s + a\Delta t^2)}{\rho_s h_s + a\Delta t^2 + \rho_f \mu_{max}}. \tag{5.3}$$

Another analysis using a generalised α method for time integration found similar criteria. [11]

The results of (5.3) and the generalised α methods corresponding to maximum and minimum numerical damping respectively can be seen in figure 5.2, when using the parameters for the tube problem. The stable region is under the graph. It is interesting to note that the three criteria are virtually identical and that a smaller time step requires a smaller ω, contrary to common engineering intuition. In the limit $\Delta t \to 0$ (5.3) becomes (5.4) where the density quota between the fluid and solid determines the behaviour.

$$0 < \omega < \frac{2}{1 + \frac{\rho_f \mu_{max}}{\rho_s h_s}}. \tag{5.4}$$

However for larger Δt the term $a\Delta t^2$ dominates, and it's primarily the stiffness combined with the time step that determines the condition on ω.

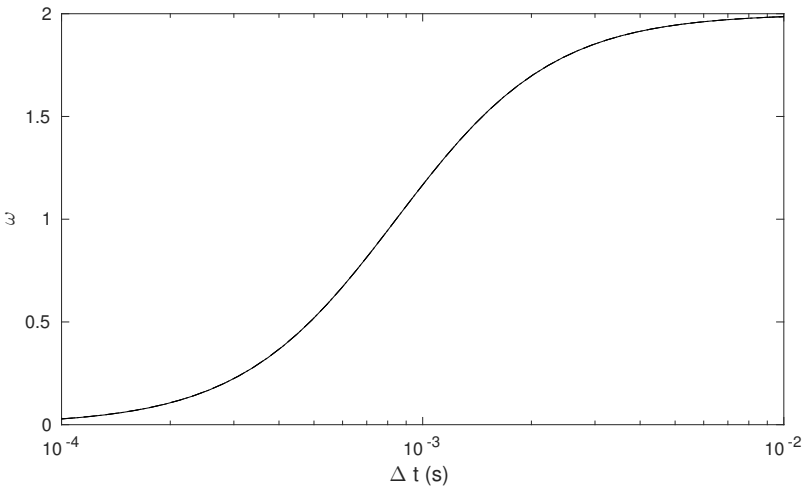

Figure 5.2: The criteria on ω for three different time integration schemes, overlaid on top of each other. The area under the graph marks the stability region.

5.2 Simplified Tube Problem

We will study a simplified mathematical model of the tube problem. Assume that the tube is made of an isotropic linear elastic material with Young's modulus E_{MD}, free to move in the axial direction in both ends, but supported and hinged in the radial and tangential directions. In reality there is a web tension giving an inhomogeneous boundary condition of the lengthwise displacement, but we will neglect that here, setting the normal force to 0 at the ends. The internal structures are neglected and the tube is filled with fluid. Other dimensions and material parameters are the same as in the numerical tube model.

The beam-like mode shapes of the tube can be classified by the indexes m and n where m is the axial mode number and n the circumferential. These can be seen in figure 5.3.

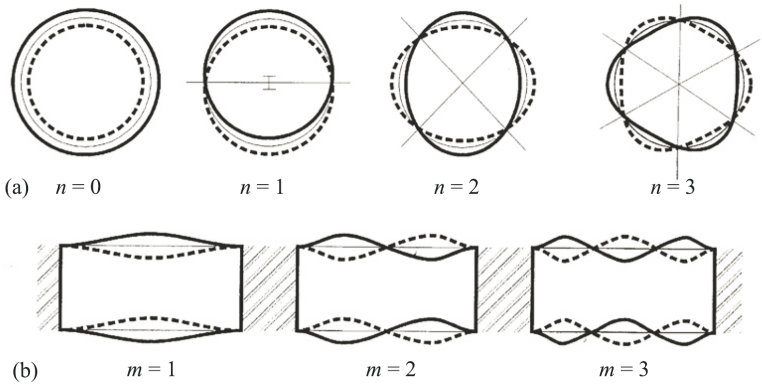

Figure 5.3: The circumferential (a) and axial (b) modes of a cylinder.

The tube walls are assumed to move radially in the mode shapes

$$U_{n,m}(x,\theta) = \sin(\frac{m\pi x}{L})\cos(n\theta) \tag{5.5}$$

where L is the tube length.

The governing equations for the tube walls was chosen to be the Love equations for cylindrical shells, a linear model for thin plates. [12]

$$\begin{cases} \rho_s h_s \ddot{W} - \frac{Eh}{1-\nu^2}\left(\frac{\partial^2 W}{\partial x^2} + \frac{1-\nu}{2r^2}\frac{\partial^2 W}{\partial \theta^2} + \frac{1+\nu}{2r}\frac{\partial^2 V}{\partial \theta \partial x} + \frac{\nu}{r}\frac{\partial U}{\partial x}\right) = p_x(\theta,x;t) \\ \rho_s h_s \ddot{V} - \frac{Eh}{1-\nu^2}\left((1+\frac{h_s^2}{12r^2})(\frac{\partial^2 V}{r^2\partial\theta^2} + \frac{1-\nu}{2}\frac{\partial^2 V}{\partial x^2}) + \frac{1+\nu}{2r}\frac{\partial^2 W}{\partial x \partial \theta} + \frac{\partial U}{r^2\partial\theta} - \frac{h_s^2}{12r^2}(\frac{\partial^3 U}{r^2\partial\theta^3} + \frac{\partial^3 U}{\partial x^2 \partial\theta})\right) = p_\theta(\theta,x;t) \\ \rho_s h_s \ddot{U} + \frac{Eh}{1-\nu^2}\left(\frac{U}{r^2} + \frac{h_s^2}{12r^2})(\frac{\partial^4 U}{r^2\partial\theta^4} + 2\frac{\partial^4 U}{\partial x^2\partial\theta^2} + r^2\frac{\partial^4 U}{\partial x^4}) + \nu\frac{\partial W}{r\partial x} + \frac{\partial V}{r^2\partial\theta} - \frac{h_s^2}{12r^2}(\frac{\partial^3 V}{\partial x^2\partial\theta} + \frac{\partial^3 V}{r^2\partial\theta^3})\right) = p_r(\theta,x;t) \end{cases} \tag{5.6}$$

W, V and U are the displacements in the axial, tangential and radial directions respectively. The added mass effect is assumed to act in the radial direction only in the following analysis.

The flow in the tube is modelled as incompressible, inviscid and irrotational which may be expressed by the linear equations 5.7.

$$\begin{cases} \rho_f \dot{\mathbf{u}} + \nabla p = 0 & \text{in } \Omega_f \\ \nabla \cdot \mathbf{u} = 0 & \text{in } \Omega_f \\ p = \bar{p}(t) & x = 0,\ x = L \\ \mathbf{u}\cdot\mathbf{n} = w & \text{on } \Sigma \end{cases} \tag{5.7}$$

which can be reformulated as (5.8).

$$\begin{cases} -\Delta p = 0 & \text{in } \Omega_f \\ p = \bar{p}(t) & x = 0,\ x = L \\ \frac{\partial p}{\partial n} = -\rho_f \dot{w} & \text{on } \Sigma \end{cases} \tag{5.8}$$

$\bar{p}$ and w are arbitrary boundary conditions, and ρ_f is the fluid density. These two sets of equations are then coupled by the conditions on the interface boundary Σ.

$$\text{on } \Sigma \begin{cases} \mathbf{u} \cdot \mathbf{n} = w = \dot{U} \\ p_r = p \end{cases} \tag{5.9}$$

This may be used to reformulate the last line of equation 5.8 as

$$\frac{\partial p}{\partial n} = -\rho_f \ddot{U} \text{ on } \Sigma \tag{5.10}$$

which means our systems of equations are fully coupled.

In order to investigate the solutions to this problem an added mass operator $\mathcal{M}_A$ is defined as (p_{ext} being a background pressure not generated by an acceleration of the walls)

$$p|_\Sigma = p_{ext} - \mathcal{M}_A \ddot{U}.$$

The existence and uniqueness of the solution using this operator are proven in the paper [9].

The real tube is filled with liquid up to a certain level H, but to simplify the analysis we will study the case where it is completely filled, i.e H=L.

We now seek the pressure p **resulting from a radial acceleration of the wall** $\ddot{U}$, and solve equation 5.8 through separation of variables.

$$p(x, \theta, r) = X(x)\Theta(\theta)R(r). \tag{5.11}$$

The Laplacian in cylindrical coordinates is

$$\Delta p = \frac{\partial^2 p}{\partial r^2} + \frac{1}{r}\frac{\partial p}{\partial r} + \frac{1}{r^2}\frac{\partial^2 p}{\partial \theta^2} + \frac{\partial^2 p}{\partial x^2} \tag{5.12}$$

Which after insertion of 5.11 becomes

$$\Delta p = X(x)\Theta(\theta)R''(r) + \frac{1}{r}X(x)\Theta(\theta)R'(r) + \frac{1}{r^2}X(x)\Theta''(\theta)R(r) + X''(x)\Theta(\theta)R(r) = 0. \tag{5.13}$$

Which implies

$$\frac{R''}{R} + \frac{1}{r}\frac{R'}{R} + \frac{1}{r^2}\frac{\Theta''}{\Theta} + \frac{X''}{X} = 0. \tag{5.14}$$

The eigenfunction Θ is by necessity the same as that of U, since it follows its movements. The axial eigenfunction depends on the boundary condition for the pressure at the outlet and inlet. A free surface or an "open" end corresponds to $p = 0$, while a "closed" boundary, i.e a solid bottom, corresponds to $\frac{\partial p}{\partial x} = 0$. [13]

Here both ends are assumed to be open and thus $X(x) = \sin(\frac{m\pi}{L}x)$ and $\Theta(\theta) = \cos(n\theta)$. This results in

$$R'' + \frac{1}{r}R' - \left(\frac{1}{r^2}n^2 + \frac{m^2\pi^2}{L^2}\right)R = 0 \tag{5.15}$$

which is known as the modified Bessel equation, and has solutions $R(r) = aI_n(\frac{m\pi}{L}r) + bK_n(\frac{m\pi}{L}r)$ where I_n and K_n are the first and second modified Bessel functions of order n respectively. Since $\lim_{r\to 0} K_n(r) \to \infty$ only I_n has to be considered. Thus p can be expanded as the function series

$$p(x,\theta,r) = \sum_{m,n} c_{m,n} \frac{I_n(\frac{m\pi}{L}r)}{I_n(\frac{m\pi}{L}r_o)} \sin(\frac{m\pi}{L}x)\cos(n\theta) \tag{5.16}$$

where the radial part has been normalised to be 1 on the wall $r = r_o$. Equation 5.10 implies

$$\frac{\partial p}{\partial r}\Big|_{r=r_o} = \sum_{m,n} c_{m,n} \frac{m\pi}{L} \frac{I_n'(\frac{m\pi}{L}r_o)}{I_n(\frac{m\pi}{L}r_o)} \sin(\frac{m\pi}{L}x)\cos(n\theta) = \sum_{i,j} -\rho_f \ddot{q}_{i,j} \sin(\frac{i\pi}{L}x)\cos(j\theta) \tag{5.17}$$

where $q_{n,m}$ is a modal coordinate dependent on time. The pressure on the wall is, due to normalisation of the radial part

$$p\Big|_{r=r_o} = \sum_{m,n} c_{m,n} \sin(\frac{m\pi}{L}x)\cos(n\theta) = -\mathcal{M}_A\ddot{U} = -\sum_{i,j} M_{i,j}\ddot{q}_{i,j} \sin(\frac{i\pi}{L}x)\cos(j\theta) \tag{5.18}$$

per definition of the added mass operator $\mathcal{M}_A$. By orthogonality of the basis functions the added mass operator is diagonal, so finding the added mass coefficients $M_{m,n}$ is relatively easy. Otherwise one would have to project the basis functions on each other which would create a coupled system of equations with densely populated matrices. Together (5.17) and (5.18) imply

$$M_{m,n} = \frac{\rho_f L}{m\pi} \frac{I_n(\frac{m\pi}{L}r_o)}{I_n'(\frac{m\pi}{L}r_o)} \tag{5.19}$$

which are the diagonal elements of $\mathcal{M}_A$.

5.3 Analysis of the HHT scheme

The HHT scheme (3.4) can be put in the following form by repeated insertion of the Newmark predictors [14]

$$\begin{aligned}
&\mathbf{M}\left[\frac{1}{\upsilon\Delta t^2}(\tilde{\mathbf{d}}^{k+1} - \mathbf{d}_n) - \frac{1}{\upsilon\Delta t}\dot{\mathbf{d}}_n - \frac{1-2\upsilon}{2\upsilon}\ddot{\mathbf{d}}_n\right] + \\
&\mathbf{C}\left[\frac{\gamma(1-\alpha)}{\upsilon\Delta t}(\tilde{\mathbf{d}}^{k+1} - \mathbf{d}_n) - \frac{\gamma(1-\alpha)-\upsilon}{\upsilon}\dot{\mathbf{d}}_n - \frac{(\gamma-2\upsilon)(1-\alpha)}{2\upsilon}\Delta t\ddot{\mathbf{d}}_n\right] + \\
&\mathbf{K}\left[(1-\alpha)\tilde{\mathbf{d}}^{k+1} - \alpha\mathbf{d}_n\right] = (1-\alpha)\mathbf{F}_{ext}(t_{n+1}) + \alpha\mathbf{F}_{ext}(t_n)
\end{aligned} \tag{5.20}$$

This assumes the nonlinear relation $\mathbf{F}_{int}(\mathbf{d})$ is evaluated by the generalized midpoint rule, and is an approximation suitable if the difference between the linearised $\mathbf{K}$-matrices is small between two time steps. If the damping matrix is nonlinear too, for example $\mathbf{C} = \beta\mathbf{K}$, the same argument applies. According to the Abaqus manual it uses the trapezoidal rule for these approximations instead, like what's done here with $\mathbf{F}_{ext}$ but for ease of analysis we will stick to the midpoint rule. We will see that this distinction doesn't matter in the following analysis, if $\mathbf{K}$ is taken as the matrix in the updated state.

Since $\mathbf{d}^{k+1} = \omega\tilde{\mathbf{d}}^{k+1} + (1-\omega)\mathbf{d}^k$ we can substitute the relaxed displacement for the predictor

$$\tilde{\mathbf{d}}^{k+1} = \frac{\mathbf{d}^{k+1}}{\omega} - \frac{1-\omega}{\omega}\mathbf{d}^k \tag{5.21}$$

in (5.20).

The fluid time integration is assumed to be a first order Euler scheme giving the acceleration $\dot{\mathbf{u}}_{n+1} = \frac{\mathbf{u}_{n+1}-\mathbf{u}_k}{\Delta t}$. Assuming first order Euler interpolation of velocity on the wall $\ddot{\mathbf{d}}_{n+1} = \frac{\mathbf{d}_{n+1}-2\mathbf{d}_n+\mathbf{d}_{n-1}}{\Delta t^2} = \dot{\mathbf{u}}_{n+1}$. Thus we can approximate the added mass effect

$$\mathbf{F}_{ext}^{k+1} = -\mathcal{M}_A \dot{\mathbf{u}}^k = -\mathcal{M}_A \frac{\mathbf{d}^k - 2\mathbf{d}_n + \mathbf{d}_{n-1}}{\Delta t^2}. \tag{5.22}$$

$\mathbf{F}_{ext}^{k+1}$ is the force imported on step $k+1$ and therefore uses the latest available information from step k, giving (5.22).

In order to write this relation on the form of a fix point iteration we are only interested in terms $k+1$ and k. The relations (5.20)-(5.22) can be compactly written in terms of the inner iteration variables $\mathbf{d}^{k+1}$, $\mathbf{d}^k$ only. Inserting the relevant terms into (5.20) yields

$$\mathbf{M}\frac{1}{\upsilon\Delta t^2}\tilde{\mathbf{d}}^{k+1} + \mathbf{C}\frac{\gamma(1-\alpha)}{\upsilon\Delta t}\tilde{\mathbf{d}}^{k+1} + \mathbf{K}(1-\alpha)\tilde{\mathbf{d}}^{k+1} = (1-\alpha)\mathbf{F}_{ext}^{k+1} + \Phi(\mathbf{d}_n, \mathbf{d}_{n-1}, \ldots) \tag{5.23}$$

which expands to

$$\begin{aligned}
&\mathbf{M}\frac{1}{\upsilon\Delta t^2}\left[\frac{\mathbf{d}^{k+1}}{\omega} - \frac{1-\omega}{\omega}\mathbf{d}^k\right] + \mathbf{C}\frac{\gamma(1-\alpha)}{\upsilon\Delta t}\left[\frac{\mathbf{d}^{k+1}}{\omega} - \frac{1-\omega}{\omega}\mathbf{d}^k\right] + \mathbf{K}(1-\alpha)\left[\frac{\mathbf{d}^{k+1}}{\omega} - \frac{1-\omega}{\omega}\mathbf{d}^k\right] \\
&= (1-\alpha)\left[-\frac{1}{\Delta t^2}\mathcal{M}_A\mathbf{d}^k\right] + \Phi(\mathbf{d}_n, \mathbf{d}_{n-1}, \ldots)
\end{aligned} \tag{5.24}$$

Equation (5.24) can be written as a fix point iteration

$$\begin{aligned}
&\left[\mathbf{M}\frac{1}{\Delta t^2} + \mathbf{C}\frac{\gamma(1-\alpha)}{\Delta t} + \mathbf{K}(1-\alpha)\upsilon\right]\mathbf{d}^{k+1} = (1-\omega)\left[\mathbf{M}\frac{1}{\Delta t^2} + \mathbf{C}\frac{\gamma(1-\alpha)}{\Delta t} + \mathbf{K}(1-\alpha)\upsilon - \frac{(1-\alpha)\omega\upsilon}{\Delta t^2(1-\omega)}\mathcal{M}_A\right]\mathbf{d}^k \\
&+ \Phi(\mathbf{d}_n, \mathbf{d}_{n-1}, \ldots)
\end{aligned} \tag{5.25}$$

Assuming the operator on the left hand side is invertible this can be written (omitting the irrelevant terms)

$$\mathbf{d}^{k+1} = \underbrace{(1-\omega)\left[I - \left[\mathbf{M}\frac{1}{\Delta t^2} + \mathbf{C}\frac{\gamma(1-\alpha)}{\Delta t} + \mathbf{K}(1-\alpha)\upsilon\right]^{-1}\frac{(1-\alpha)\omega\upsilon}{\Delta t^2(1-\omega)}\mathcal{M}_A\right]}_{\mathcal{J}}\mathbf{d}^k \tag{5.26}$$

The inner iteration is asymptotically stable if and only if the absolute value of the maximal eigenvalue of $\mathcal{J} < 1$. Let $(\cdot)_{max}$ symbolise the maximum eigenvalue, then $(\mathcal{J})_{max} < 1$ which means

$$\left|(1-\omega)\left[1 - \frac{(1-\alpha)\omega\upsilon}{\Delta t^2(1-\omega)}\left(\left[\mathbf{M}\frac{1}{\Delta t^2} + \mathbf{C}\frac{\gamma(1-\alpha)}{\Delta t} + \mathbf{K}(1-\alpha)\upsilon\right]^{-1}\mathcal{M}_A\right)_{max}\right]\right| < 1 \tag{5.27}$$

Inserting $\gamma = \frac{1}{2} + \alpha$ and $\upsilon = \frac{1}{4}(1+\alpha)^2$ yields

$$\begin{aligned}
&\frac{(1-\alpha)\omega\upsilon}{\Delta t^2(1-\omega)}\left(\left[\mathbf{M}\frac{1}{\Delta t^2} + \mathbf{C}\frac{\gamma(1-\alpha)}{\Delta t} + \mathbf{K}(1-\alpha)\upsilon\right]^{-1}\mathcal{M}_A\right) = \\
&\frac{\omega}{1-\omega}\left(\left[\mathbf{M}\frac{4}{(1-\alpha)(1+\alpha)^2} + \mathbf{C}\frac{4\Delta t(\frac{1}{2}+\alpha)}{(1+\alpha)^2} + \mathbf{K}\Delta t^2\right]^{-1}\mathcal{M}_A\right)
\end{aligned} \tag{5.28}$$

And assuming $\mathbf{C} = \beta\mathbf{K}$ we get

$$= \frac{\omega}{1-\omega}\left(\left[\mathbf{M}\frac{4}{(1-\alpha)(1+\alpha)^2} + \mathbf{K}\left(4\beta\frac{\Delta t(\frac{1}{2}+\alpha)}{(1+\alpha)^2} + \Delta t^2\right)\right]^{-1}\mathcal{M}_A\right).$$

Thus the condition on ω is

$$\left|1-\omega-\omega\left(\left[\mathbf{M}\frac{4}{(1-\alpha)(1+\alpha)^2} + \mathbf{K}\left(4\beta\frac{\Delta t(\frac{1}{2}+\alpha)}{(1+\alpha)^2} + \Delta t^2\right)\right]^{-1}\mathcal{M}_A\right)_{max}\right| < 1. \tag{5.29}$$

The mass matrix $\mathbf{M}$ is positive definite, $\mathcal{M}_A$ positive (semi)-definite, and $\mathbf{K}$ is generally positive semidefinite, unless severe nonlinearities occur, which we will neglect here. The criterion can be written

$$0 < \omega < \frac{2}{1+\left(\left[\mathbf{M}\frac{4}{(1-\alpha)(1+\alpha)^2} + \mathbf{K}\left(4\beta\frac{\Delta t(\frac{1}{2}+\alpha)}{(1+\alpha)^2} + \Delta t^2\right)\right]^{-1}\mathcal{M}_A\right)_{max}} \tag{5.30}$$

5.4 Application to the Tube Problem

The tube is fixed but hinged in the radial- and tangential directions at both ends, but free to move in the lengthwise direction at both ends. Therefore we assume the modes of the U, V, W-displacements to be

$$\begin{cases} U_{m,n} = u_{m,n}\sin(\frac{m\pi x}{L})\cos(n\theta) \\ V_{m,n} = v_{m,n}\sin(\frac{m\pi x}{L})\sin(n\theta) \\ W_{m,n} = w_{m,n}\cos(\frac{m\pi x}{L})\cos(n\theta) \end{cases} \tag{5.31}$$

These mode shapes are motivated in [12]. Note that the mode shape for $W_{m,n}$ is not really consistent with physical reality since there can be no normal forces in the x-direction couteracting the web tension under these assumptions. $\mathcal{N}_{xx}|_{x=0} \propto (\frac{\partial W}{\partial x} + \nu(\frac{\partial V}{r\partial\theta} + \frac{U}{r}))|_{x=0} \Rightarrow \frac{\partial W}{\partial x}|_{x=0} = 0$. However this was part of the simplifications made in order to be able to treat the problem easily. Hopefully this system can yield some insights into the physical behaviour. Projecting the mode shapes 5.31 on Love's equations yields the uncoupled system of equations (5.32) in modal coordinates. [12] This is valid under the assumption that the pressure eigenfunctions are the same as the displacement eigenfunctions, which is true in our case.

$$\frac{Eh_s}{1-\nu^2}\begin{pmatrix} K_{11} & K_{12} & K_{13} \\ K_{21} & K_{22} & K_{23} \\ K_{31} & K_{32} & K_{33} \end{pmatrix}\begin{pmatrix} w_{m,n} \\ v_{m,n} \\ u_{m,n} \end{pmatrix} + \rho_s h_s \begin{pmatrix} 1 & 0 & 0 \\ 0 & 1 & 0 \\ 0 & 0 & 1 \end{pmatrix}\begin{pmatrix} \ddot{w}_{m,n} \\ v_{m,n} \\ u_{m,n} \end{pmatrix} = \begin{pmatrix} p_x \\ p_\theta \\ p_r \end{pmatrix}_{m,n} \tag{5.32}$$

where

$$\begin{cases} K_{11} = \left(\frac{m\pi}{L}\right)^2 + \left(\frac{1-\nu}{2}\right)\left(\frac{n}{r}\right)^2 \\ K_{22} = (1 + \frac{h_s^2}{12r^2}\left(\left(\frac{n}{r}\right)^2 + \frac{1-\nu}{2}\left(\frac{m\pi}{L}\right)^2\right) \\ K_{33} = \frac{1}{r^2} + \frac{h^2}{12}\left(\left(\frac{n}{r}\right)^2 + \left(\frac{m\pi}{L}\right)^2\right)^2 \\ K_{12} = K_{21} = -\frac{1+\nu}{2}\frac{n}{r}\frac{m\pi}{L} \\ K_{13} = K_{31} = -\frac{\nu}{r}\frac{m\pi}{L} \\ K_{23} = K_{32} = n\left(\frac{1}{r^2} + \frac{h_s^2}{12r^2}\left(\left(\frac{n}{r}\right)^2 + \left(\frac{m\pi}{L}\right)^2\right)\right) \end{cases} \tag{5.33}$$

Assuming that the added mass effect only acts in the radial direction, the pressures can be written in terms of added mass, again due to the orthogonality of the eigenfunctions

$$\begin{pmatrix} p_x \\ p_\theta \\ p_r \end{pmatrix}_{m,n} = \begin{pmatrix} 0 \\ 0 \\ -M_{m,n}\ddot{u}_{m,n} \end{pmatrix} \tag{5.34}$$

The governing equations for the simplified problem can now be written

$$\begin{pmatrix} \mathbf{K}_{m_1,n_1} & 0 & \dots & 0 \\ 0 & \mathbf{K}_{m_1,n_2} & \dots & 0 \\ \vdots & 0 & \ddots & \vdots \\ 0 & \dots & 0 & \ddots \end{pmatrix} \begin{pmatrix} w_{m1,n1} \\ v_{m1,n1} \\ u_{m1,n1} \\ w_{m1,n2} \\ \vdots \end{pmatrix} + \rho_s h_s \mathbf{I} \begin{pmatrix} \ddot{w}_{m1,n1} \\ \ddot{v}_{m1,n1} \\ \ddot{u}_{m1,n1} \\ \ddot{w}_{m1,n2} \\ \vdots \end{pmatrix} = \begin{pmatrix} 0 & 0 & 0 & \dots & 0 \\ 0 & 0 & 0 & \dots & 0 \\ \vdots & 0 & -M_{m_1,n_1} & \dots & \vdots \\ 0 & \dots & 0 & \ddots & 0 \end{pmatrix} \begin{pmatrix} \ddot{w}_{m1,n1} \\ \ddot{v}_{m1,n1} \\ \ddot{u}_{m1,n1} \\ \ddot{w}_{m1,n2} \\ \vdots \end{pmatrix}. \tag{5.35}$$

Adding a stiffness proportional β damping and discretising the problem in time with the HHT scheme, the criterion 5.30 becomes

$$0 < \omega < \inf_{m,n} \frac{2}{1 + \left(\left[\rho_s h_s \mathbf{I} \frac{4}{(1-\alpha)(1+\alpha)^2} + \mathbf{K}_{m,n} \left(4\beta \frac{\Delta t(\frac{1}{2}+\alpha)}{(1+\alpha)^2} + \Delta t^2 \right) \right]^{-1} \begin{pmatrix} 0 & 0 & 0 \\ 0 & 0 & 0 \\ 0 & 0 & M_{m,n} \end{pmatrix} \right)_{max}} \tag{5.36}$$

Since the matrices in 5.35 are block diagonal, their inverses are also block diagonal, and the problem can be transferred into finding the mode m, n that puts the greatest limitations on ω via (5.36). This is utimately thanks to the possibility to associate a stiffness and added mass to each mode, independent of other modes.

The critical ω for $n \in [0, 2],\ m \in [1, 2]$ are plotted in figure 5.4. For reference, higher modes have been left out since they are all in the upper part of the graph. See figure 5.5 for all modes $n \in [0, 20],\ m \in [1, 20]$. The area under the graph should be considered the domain of stable combinations of Δt and ω for the model problem, and the region over the graph unstable. In this case stability seems to be limited by the added mass effect on the mode $m = 1,\ n = 1$.

5.5 Correspondence to the Numerical Case

5.5.1 Validation of the Stability Criterion

The model problem deviates from the full case on several points. Anisotropy and web tension is neglected, there is no fill pipe or pressure flange and maybe the most striking is the free surface. In order to investigate the validity of the criterion found for the model problem, the base case was run with a filled tube. The results are seen in table 5.1 and a comparison to the results in the previous section is available in figure 5.6. It was noted if the simulations became unstable and if so when. One simulation crashed after running for a while, and this will be interpreted as being close to the critical parameter ω and will be marked *uncertain*. The correspondence to the theoretical results in figure 5.4 seems to be good. Note that using a grid flux URF of 0.7 permitted running $\Delta t = 0.5$ ms and $\omega = 0.3$, which should theoretically be unstable, and was also shown to be unstable when increasing the grid flux URF to 1. This behaviour supports the anecdotal evidence and previous experiences that grid flux under-relaxation helps stabilise the algorithm.

Running a filled tube case with $\Delta t = 2$ ms and $\omega = 0.65$ caused instabilities, just as the criterion 5.4 predicts. The behaviour just before the crash was a displacement of increasing amplitude in the

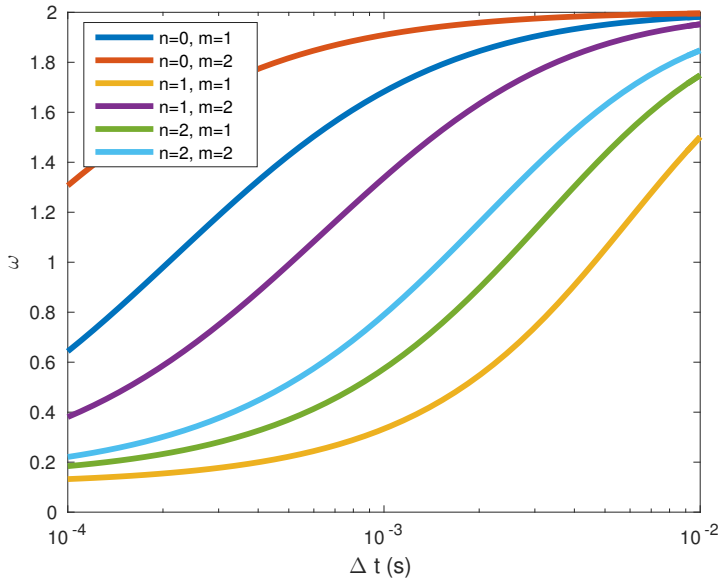

Figure 5.4: The critical displacement under-relaxation factor for different modes m, n in the base case, calculated from the parameters in the model problem (5.35).

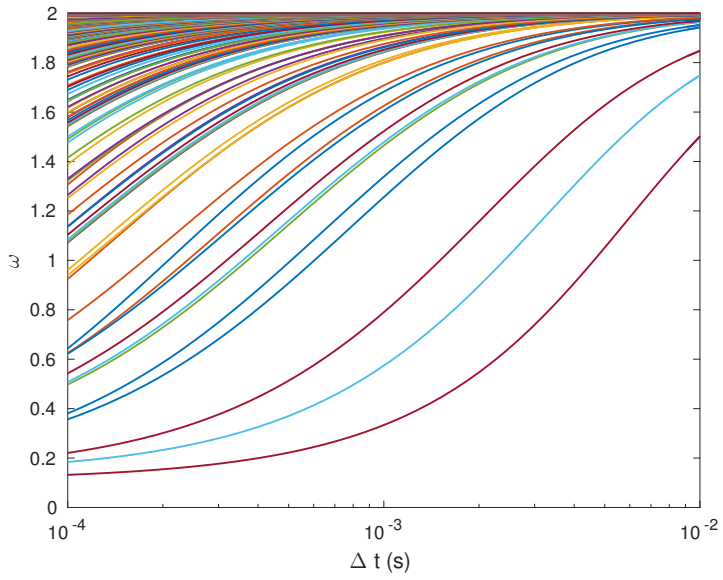

Figure 5.5: The critical displacement under-relaxation factor for all modes $m, n \leq 20$.

mode $m = 1, n = 1$, and a magnified vector warp of the tube at the crash can be seen in figure 5.7. This behaviour seems to confirm the theoretical prediction that it is the mode $m = 1,\ n = 1$ that is sensitive to the added mass effect for these parameter choices.

The same behaviour was observed in other simulations, for example $\Delta t = 4$ ms, $\omega = 0.85$ and grid flux 1. The convergence criterion on the surface average incremental displacement was observed to first go down nicely, then growing and diverging. See figure 5.8. A possible explanation for this behaviour is that during the ramp-up period the pressure and thus the added mass effect suddenly became large enough to start to amplify any errors in the mode $n = 1, m = 1$ in the fix point iteration, and this is what we see in the picture.

In order to study the model problem's applicability to the original half filled tube a number of

Δt (ms)	ω	Grid Flux	Behaviour	Verdict
0.5	0.3	0.7	Ran up to 0.65 t_{sim}, stopped manually	Stable
0.5	0.3	1	Unstable after 0.95 t_{ramp}	Unstable
0.5	0.15	1	Hit pressure flange at 0.65 t_{sim}	Stable
2	0.8	0.7	Unstable after 0.84 t_{ramp}	Unstable
2	0.4	1	Hit pressure flange at 0.64 t_{sim}	Stable
2	0.65	1	Unstable after 0.82 t_{ramp}	Unstable
4	0.95	1	Unstable after 0.76 t_{ramp}	Unstable
4	0.85	1	Unstable after 0.8 t_{ramp}	Unstable
4	0.7	1	Unstable very soon after t_{ramp}	Unstable
4	0.6	1	Unstable after 0.25 t_{sim}	Uncertain
4	0.55	1	Hit pressure flange at suction 2	Stable

Table 5.1: The outcome of simulations with a filled tube.

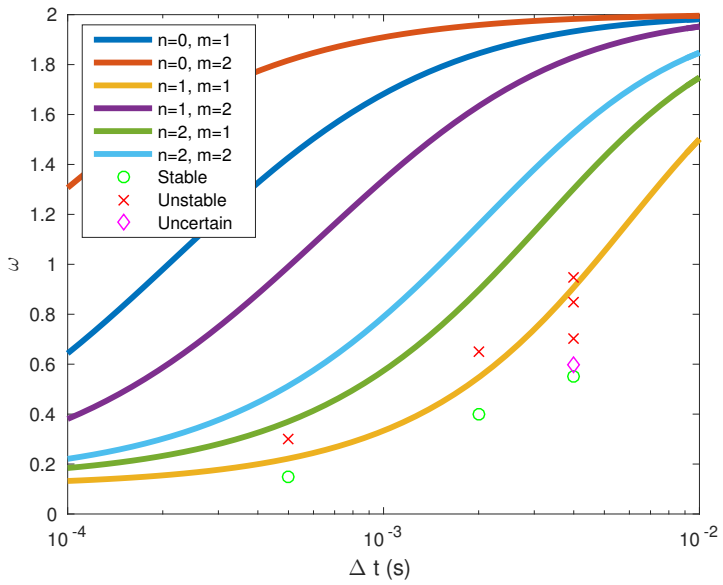

Figure 5.6: The simulations in table 5.1 compared to the theoretical stability domain predicted by (5.36).

Figure 5.7: A magnified vector warp of the displacements just before a crash. The mode $m = 1,\ n = 1$ can be identified.

simulations were run, starting from the base case with a free surface. These are listed in table 5.2 and plotted against the stability domain for the model problem in figure 5.9.

The condition on ω seems to be less strict with a free surface than for the filled tube, making the base case more stable. Even though the cases in 5.2 use grid flux under-relaxation 0.7 the point $\Delta t = 2$ ms, $\omega = 0.8$ with grid flux under-relaxation 0.7 was unstable in 5.1 but not for the half-filled tube.

Considering that the parameters of the base case are completely arbitrary from the point of view of the governing equations, the findings support the applicability of (5.36). The assumptions of

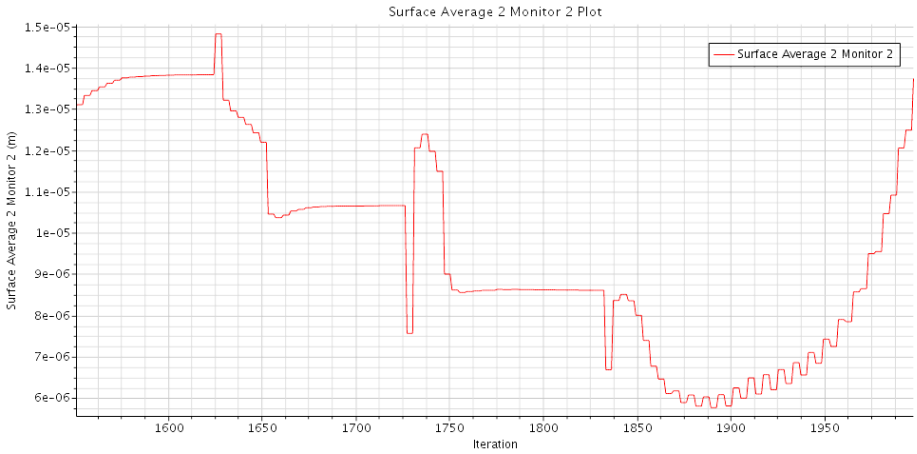

Figure 5.8: The surface average incremental displacement at a crash. The sudden onset of instability is seen around iteration 1850.

Δt (ms)	ω	Behaviour	Verdict
0.5	0.3	Finished t_{sim}	Stable
0.5	0.8	Unstable at 1st time step	Unstable
1	0.8	Unstable after $0.3t_{sim}$	Uncertain
1	0.5	Finished t_{sim}	Stable
2	0.8	Hit flange wall at $0.65t_{sim}$	Stable
5	0.8	Hit flange wall at $0.65t_{sim}$	Stable

Table 5.2: The outcome of simulations on the original problem with a free surface.

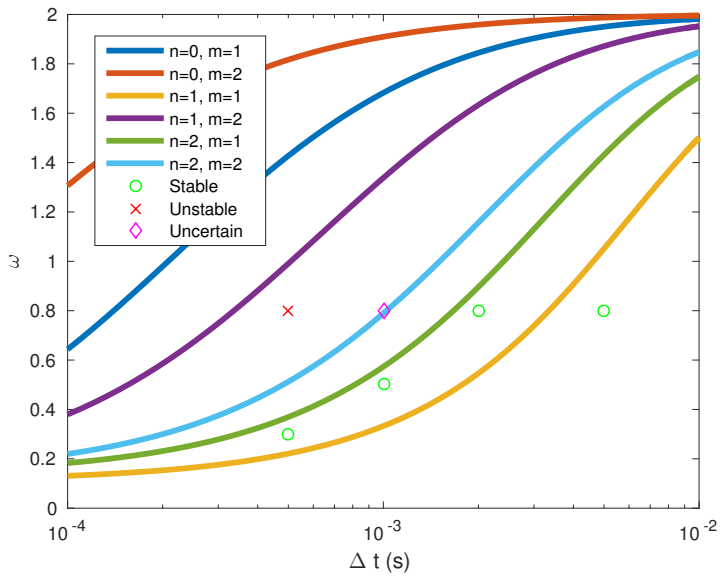

Figure 5.9: The simulations on the original tube problem in table 5.2 compared to the theoretical stability domain predicted by (5.36).

unconstrained potential flow in a tube of isotropic material of the higher Young's modulus E_{MD} should under-predict the numerical difficulties. Note that the two-dimensional model can not predict instability as it would correspond to the modes $n = 0$. Neither can the simplification in [9] of using only the maximal eigenvalue of the added mass matrix be employed, since in this case $(\mathcal{M}_A)_{max} = M_{n=0,m=1} \approx 4200$ but $M_{n=1,m=1} \approx 26$, and thus the added mass effect would be vastly

over-estimated, giving an overly conservative criterion on ω. The point of this analysis is thus to balance the stiffness and added mass effect for each mode to be able to account for deformations and translations of the cross section of the tube. The analysis in [9] is valid when the modes $n = 0$ dominate the behaviour, as perhaps in the blood vessel the authors sought to model.

5.5.2 Spectral Analysis

In noting that equation 5.35 can be seen as a modal equation

$$\frac{1}{\rho_s h_s}\mathbf{K}_{m,n} - \omega^2 \mathbf{I} = 0 \tag{5.37}$$

the eigenfrequencies can be extracted, and the lowest frequency in vacuum for each mode is seen in table 5.3, compared to the respective modes calculated from the Abaqus case.

m \ n	0	1	2	3
1	1222	160	220	538
2	2444	586	290	547

(a) The eigenfrequencies of the model problem.

m \ n	0	1	2	3
1	-	223	137	325
2	-	665	265	345

(b) The eigenfrequencies calculated in the numerical case.

Table 5.3: The calculated eigenfrequencies $f = \omega/2\pi$ (Hz).

Identifying a modal stiffness coefficient $k_{m,n} = \rho_s h_s \omega_{m,n}^2$ one could argue that higher frequencies correspond to stiffer modes, allowing for higher displacement under-relaxation factors and vice versa. Therefore it is important to note that the mode $n = 1,\ m = 1$ seems to be stiffer in the real case than the model predicts, and $n = 2,\ m = 1$ is less stiff. These two are the most critical modes according to the model problem 5.4, so the discrepancy may have an effect on the validity of conclusions drawn from the model problem.

5.6 Numerical Calculations of The Stability Criteria

One can do numerically what was done analytically in the previous section, using the actual FEM matrices, and finding the real added mass matrix for the geometry at hand, including the fill pipe, pressure flange and free surface.

Denote $\mathbf{K} = \mathbf{K}_0 + \mathbf{K}_P$ where $\mathbf{K}_0$ stands for the constant initial matrix in the finite element formulation, and $\mathbf{K}_P$ for the nonlinear contribution. Consider the linear problem

$$\mathbf{M}\ddot{\mathbf{d}} + \mathbf{C}\dot{\mathbf{d}} + \mathbf{K}_0\mathbf{d} = \mathbf{F}.$$

A standard technique in linear structural dynamics is modal decomposition.

Let Φ_i be a solution to the generalized eigenvalue problem

$$\omega_i^2 \mathbf{M}\mathbf{d} = \mathbf{K}_0\mathbf{d}.$$

A change of basis to $\Phi_1,\ \Phi_2 \ldots$ turns the linear problem into

$$\Phi^T\mathbf{M}\Phi\ddot{\mathbf{q}} + \Phi^T\mathbf{C}\Phi\dot{\mathbf{q}} + \Phi^T\mathbf{K}_0\Phi\mathbf{q} = \Phi^T\mathbf{F} \tag{5.38}$$

where $\mathbf{q} = \Phi^T\mathbf{d}$ are the modal coordinates, i.e $\mathbf{q} = (1, 0, 0 \ldots)^T$ is the coordinate of the first eigenmode of the system and so on, and Φ is the matrix consisting of the normalised eigenvectors Φ_i as columns. The matrices on the left hand side are all diagonal, allowing for easy manipulation, and $\Phi^{-1} = \Phi^T$.

The added mass matrix can be calculated by solving Laplace's equation in the domain with boundary conditions $p = 0$ at the surface, the walls above, the fill pipe, the outlet and the inlet, and $\frac{\partial p}{\partial n} = -\rho_f \Phi_i$ on the walls below. This can be done in any numerical PDE solver capable of solving the heat transfer equations or electrostatics. This calculation can be done for a subset S of the eigenvectors Φ_i, where the spanning matrix is Φ_S. The pressure field obtained for different i can be gathered in a matrix Ψ such that $\mathcal{M}_A \Phi_S = \Psi_S$.

The system 5.38 can then be projected down on this subset of eigenvectors by multiplication from the left and right.

$$\Phi_S^T \mathbf{M} \Phi_S \ddot{\mathbf{q}}_S + \Phi_S^T \mathbf{C} \Phi_S \dot{\mathbf{q}}_S + \Phi_S^T \mathbf{K}_0 \Phi_S \mathbf{q}_S = -\Phi_S^T \mathcal{M}_a \ddot{\mathbf{d}}_S = -\Phi_S^T (\Psi_S \Phi_S^T)(\Phi_S \ddot{\mathbf{q}}_S) = -\Phi_S^T \Psi_S \ddot{\mathbf{q}}_S \quad (5.39)$$

If a suitable subset S of eigenmodes has been chosen one can expect the eigenvector corresponding to the maximal eigenvalue of (5.30) to be close to a vector in the subspace. We can therefore seek out the maximal eigenvalue in the subspace instead, and calculate

$$\left(\left[\Phi_S^T \mathbf{M} \Phi_S \frac{4}{(1-\alpha)(1+\alpha)^2} + \Phi_S^T \mathbf{K} \Phi_S (4\beta \frac{\Delta t(\frac{1}{2}+\alpha)}{(1+\alpha)^2} + \Delta t^2) \right]^{-1} \Phi_S^T \Psi_S \right)_{max}$$

Note that this can be calculated over time while updating the $\mathbf{K}$ matrix to see if nonlinear effects of the finite element formulation affect the stability.

5.6.1 An Easier Way

Given a certain simulation setting with a fixed β, Δt etc, one could ramp up the pressure on the walls linearly over a certain period $0 \leq t \leq t_{ramp}$ and note the fraction $t/t_{ramp} = c$ when the simulation becomes unstable, using an initial guess for the displacement URF ω_0. Then the critical added mass for that setting should be $c\mathcal{M}_A$. An estimate for ω is the solution to the system

$$\begin{cases} \omega_0 = \frac{2}{1+xc} \\ \omega = \frac{2}{1+x} \end{cases} \quad (5.40)$$

which is

$$\omega = \frac{2\omega_0 c}{\omega_0(c-1)+2}.$$

Of course this is only an approximation, and it would be smart to set ω lower. The test should be done with numerically difficult boundary conditions in order to avoid surprises later.

Chapter 6

Discussion

In this section the effect of the added mass on the instability is discussed, and some other phenomena that may affect the stability. An effort to find suitable parameters for future simulations is also made, and the contact condition is discussed.

6.1 Numerical Results

6.1.1 β Damping

Increasing β successively damps out the dynamics of the solution, and it is clear from figures 4.6-4.8 that the solution using $\beta = 0.004$ will be very different from $\beta = 0$. The critical damping frequency might provide some estimates for setting β to a value that will filter out high frequencies but not the overall behaviour of the tube, according to figure 3.5. It may be surprising that the tube hit is barely damped out while the suction peaks are, even though their periods are practically the same. Looking at the maximum wall displacement one can see that the tube hit is much smaller than the suction peaks, and this would mean that the overall velocity involved in the suction is higher than the tube hit, causing larger damping forces.

6.1.2 Grid Flux

One can see that the grid flux under-relaxation definitely affects the solution, but it is surprising that there does not seem to be a simple relation between the amount of under-relaxation and the damping effect. In figures 4.9-4.11 this strange behaviour is demonstrated. The arbitrarily chosen grid flux URF 0.7 for the base case caused us to miss a peak towards the end of the cycle, and due to the erratic effect on the solution it seems next to impossible to estimate what goes missing for a certain grid flux URF.

6.1.3 Time Discretisation Order

The time discretisation did not look like it affected the solution much in the first three plots 4.12-4.14, but looking at the radial displacement a clear difference can be discerned in figure 4.15. The first order scheme seems to have larger displacements in this probe point, which is a bit surprising as it is normally more dissipative than the second order scheme. This may be a local effect. Otherwise the solutions have roughly the same overall behaviour, with differences in the amplitude of peaks and small oscillations.

6.2 Parameter Variations

Denote the original quantities in the base case for the model problem L_0, r_0, ρ_{s0} etc. These parameters will be varied in equation 5.36 and the corresponding ω plotted and compared to the base case which is marked with grey dashed lines.

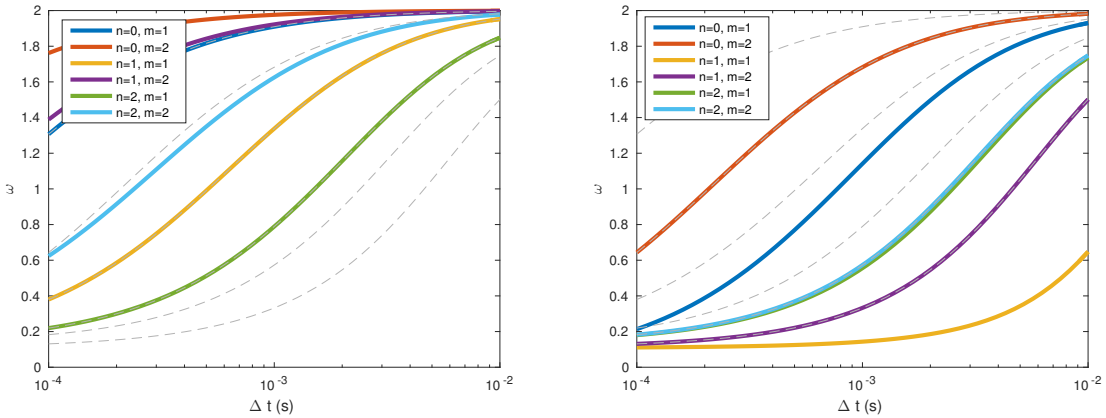

Figure 6.1: Tube length L. To the left $\frac{1}{2}L_0$, to the right $2L_0$.

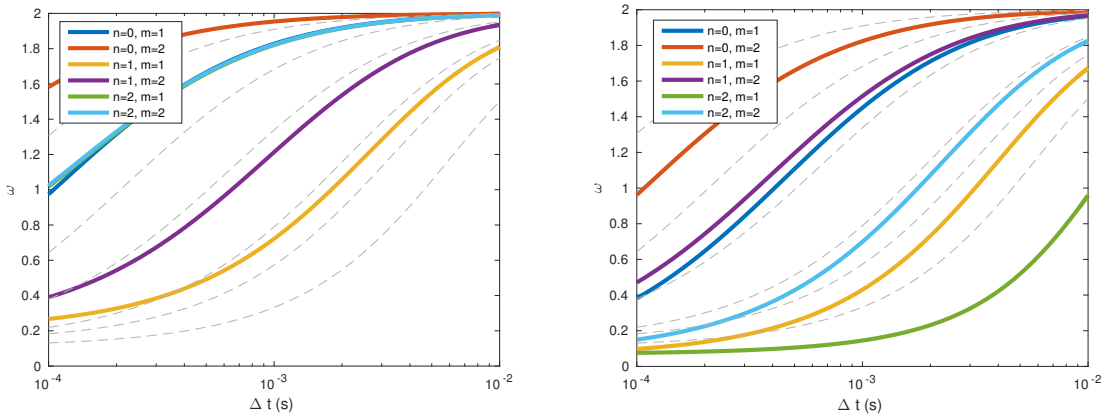

Figure 6.2: Tube radius r. To the left $\frac{1}{2}r_0$, to the right $2r_0$.

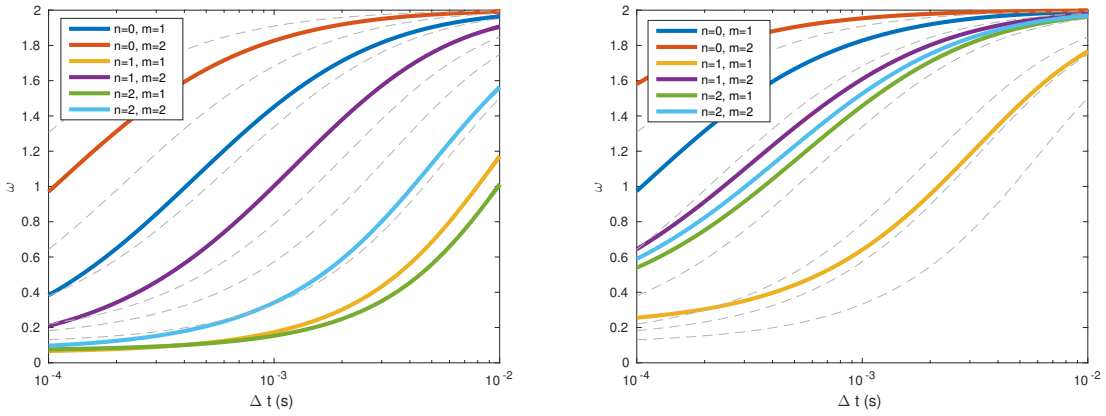

Figure 6.3: Wall thickness h_s. To the left $\frac{1}{2}h_{s0}$, to the right $2h_{s0}$.

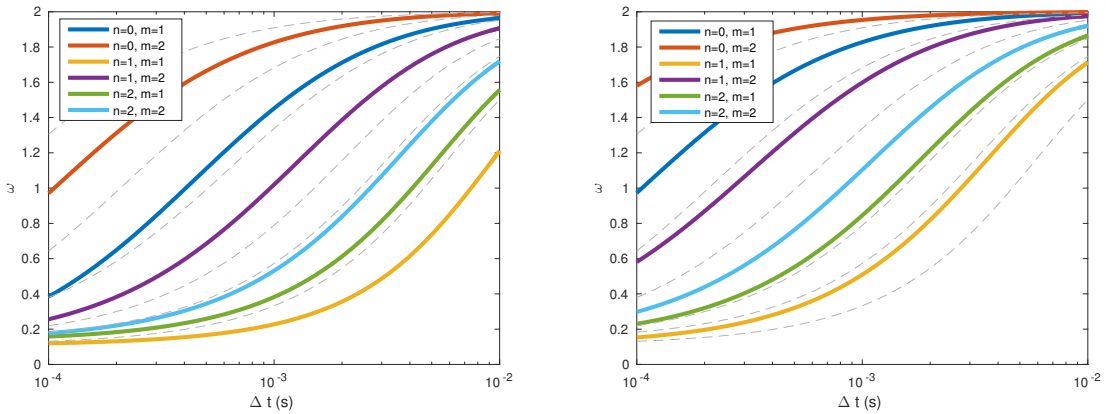

Figure 6.4: Young's modulus E. To the left $\frac{1}{2}E_0$, to the right $2E_0$.

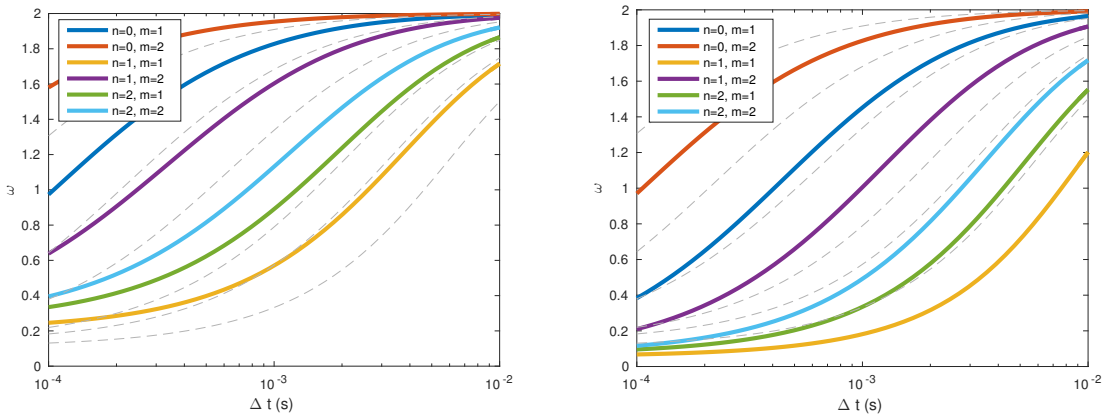

Figure 6.5: Fluid density ρ_f. To the left $\frac{1}{2}\rho_{f0}$, to the right $2\rho_{f0}$.

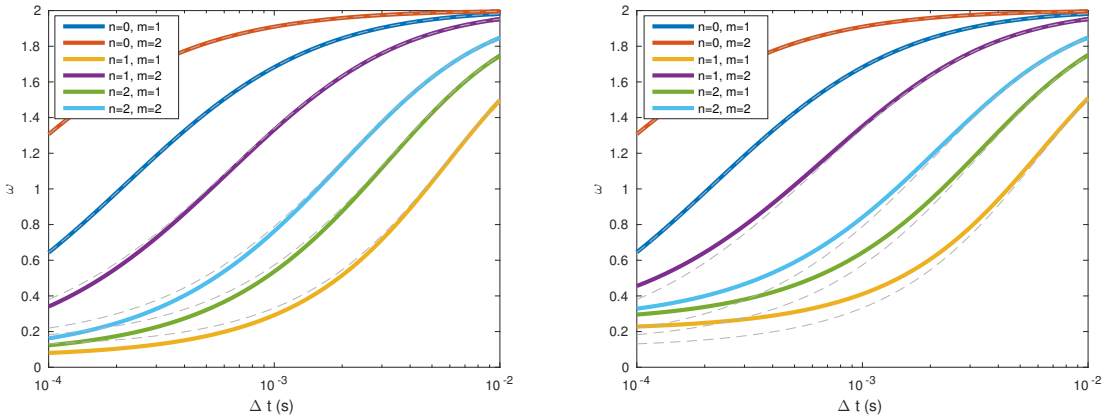

Figure 6.6: Solid density ρ_s. To the left $\frac{1}{2}\rho_{s0}$, to the right $2\rho_{s0}$.

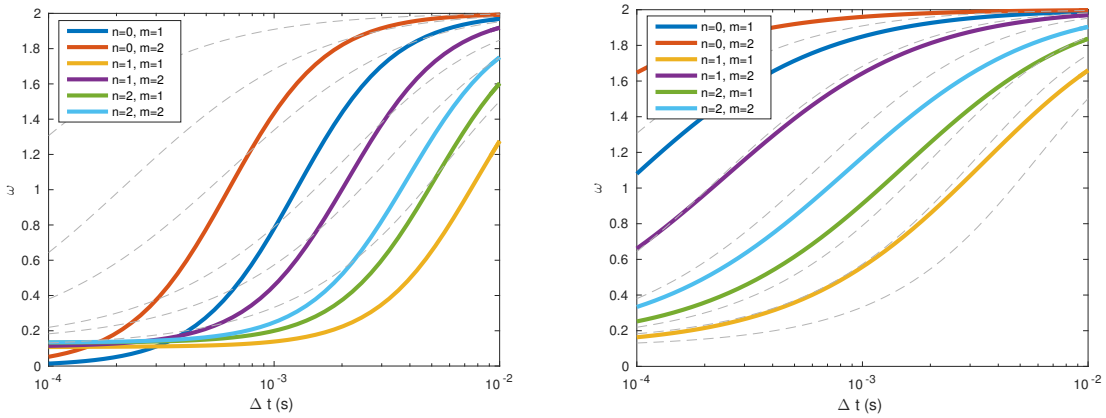

Figure 6.7: Rayleigh damping β. To the left $\beta = 0$, to the right $\beta = 0.01$.

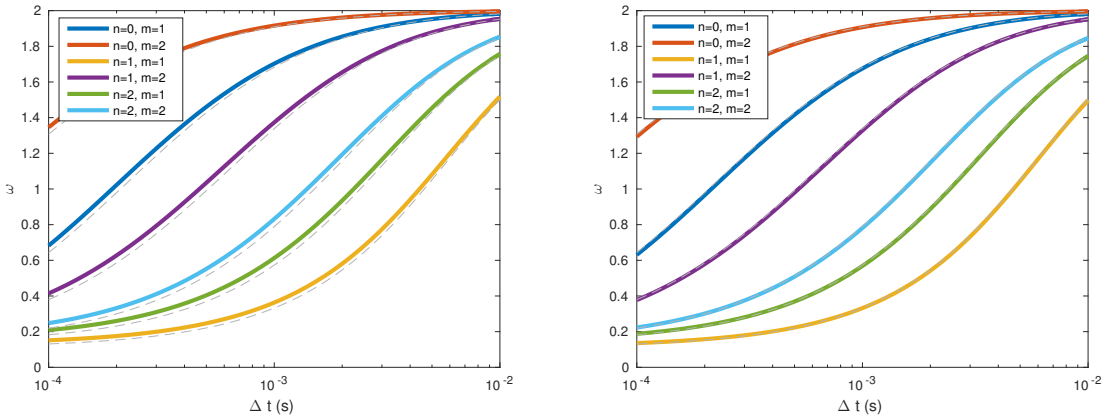

Figure 6.8: Numerical dissipation α in the HHT scheme. To the left $\alpha = 0$, to the right $\alpha = 0.5$.

Clearly (5.36) predicts that the added mass instability gets worse for long or wide tubes, heavy fluids, thin walls, and low Young's modulus. The β damping seems to have a very beneficial effect on the stability as experience indicates, especially for smaller time steps. The numerical dissipation parameter α seems to have very little effect, and so does ρ_s, except for in the limit $t \to 0$ where high material densities increase the minimum ω analogously to (5.4).

6.3 Effects of Water/Air Surface

The model problem assumes a filled tube which is not the case in the practical simulations. There are some uncertainties surrounding the effect of the surface on stability. On the one hand less water is displaced which should decrease the added mass effect, but there will be splashes and surface waves giving rise to nonlinear and unpredictable phenomena.

The surface also changes the natural mode shapes. For example consider a partitioned system where the canonical equation becomes

$$\left[\begin{pmatrix} K_{gg} & K_{gl} \\ K_{lg} & K_{ll} \end{pmatrix} - \omega^2 \begin{pmatrix} M_{gg} & M_{gl} \\ M_{lg} & M_{ll} + \mathcal{M}_A \end{pmatrix}\right] \begin{pmatrix} \mathbf{d}_g \\ \mathbf{d}_l \end{pmatrix} = 0 \tag{6.1}$$

where index g stands for gas and l for liquid respectively. This system of equations does not generally have the same solutions as the modal equations in vacuum $\mathcal{M}_A = 0$, depending on if the pressure eigenfunctions are the same as the modes or not, which is generally not true in case of a surface. In this case there will be cross-couplings of the eigenmodes of the pressure and the displacement, maybe effectively increasing the added mass effect in some modes and decreasing it in others, also depending on the current fluid level. Figures 5.6 and 5.9 indicate that the free surface case is more stable than the filled tube.

6.4 Effects of Geometry

Païdoussis [15] studies the fluid-structure coupling of infinitely long annular tubes conducting fluid in the middle channel. In the case of an outer tube of radius R_o vibrating in the transversal mode $n = 1$, with a fixed inner tube of radius R_i, the added mass force per unit length in this mode depends of the ratio of the radii. The multiplication constant C_m can be seen in figure 6.9. As can be seen the effect of a narrow gap is an enormous increase in added mass. In the tube case the fill pipe acts as an inner cylinder, which gives a ratio R_o/R_i varying between approximately $1.01 \Rightarrow C_m \approx 70$ and $\infty \Rightarrow C_m \approx 1$. This introduces a lot of uncertainty in every estimate of the added mass matrix, and it may introduce large local effects.

Additionally the movement of the walls will change the gap distance over time which gives the added mass effect an extremely nonlinear behaviour locally. In the simulations of the full geometry the fill pipe and floater are also allowed to move, which may have a synergistic effect on the added mass if it should happen to oscillate in tune with the walls, in addition to making the fluid gap even smaller at times. [15]

These kinds of effects may explain instabilities where the solution is stable for the whole ramp-up period, runs for some time and then becomes unstable when the walls start to deform, closing the fluid gap and increasing the local added mass effect, typically during suction. Cases where the walls run into the pressure flange may be caused by this phenomenon rather than the walls hitting the flange as part of a purely dynamical procedure. In that case, the β damping that reduces the displacement will also reduce these effects, contributing further to the overall stability.

6.5 Effects of Viscosity

Just as there is an added mass, there may be an added viscous force related to the wall movements. Païdoussis goes on to derive an expression for the coupling force considering viscous flow. For a

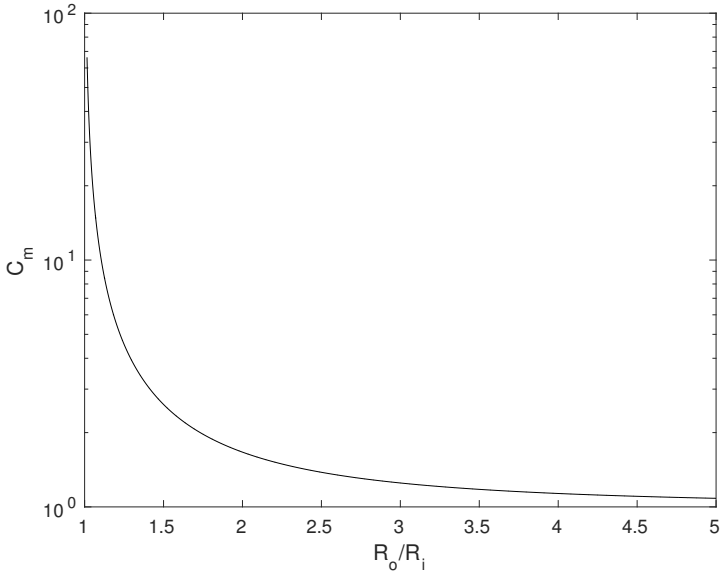

Figure 6.9: The added mass coefficient for the transversal motion of a vibrating tube of radius R_o containing a fixed tube of radius R_i.

certain vibrational mode the viscous force can be written $F_v = -C_d \Omega \rho_f A \dot{z}$ where z is a coordinate, Ω is an oscillation frequency and C_d is positive and given by a very complex expression. This constant exhibits a behaviour similar to C_m with varying diameters. For the details, see section 2.2.4 in [15].

Since the viscosity will act as a reaction force analogous to the added mass one can expect highly viscous flows to be harder to handle, and require lower ω. The force is proportional to the wall velocity, and thus one can hypothesise that the added viscosity will act as an addition to (5.22) which would consequently modify (5.30) where $\mathcal{M}_A$ should be replaced by $(\mathcal{M}_A + \Delta t \mathcal{V}_A)$ for some added viscosity operator $\mathcal{V}_A$, and the factor Δt is due to the velocity dependence as opposed to the added mass' acceleration dependence. Thus viscous effects should be more severe for larger time steps, which could explain the behaviour in figure 5.6 where larger time steps seem to be relatively difficult compared to the predicted stability region.

6.6 Effects of Compressibility

There is a fundamental difference between the added mass concepts for compressible and incompressible fluids. The added mass is a certain portion of the fluid pushing back on the wall as a reaction force resulting from the wall accelerations. However, if we consider an acceleration of the wall at time t_0, this information spreads instantaneously throughout the whole domain in the incompressible case, while for the compressible flow, the maximum radius of influence is $c\Delta t$, where c is the speed of sound in the fluid, and Δt the time interval. For small discrete time steps this yields a characteristic length limiting the added mass to $m_f \propto c\Delta t \rho_f$. [16]

This should be taken to be valid in the limit $\Delta t \to 0$. For example, with a speed of sound $c = 600$ m/s and a time step $\Delta t = 5 \cdot 10^{-4}$ s the radius of influence is $c\Delta t \approx 0.3$ m which is more than 10 times the radius of the tube and about half its length. However, considering an explicit scheme the criterion $\frac{\rho_s h_s}{\rho_f \mu_{max}} < C$ outlined in [10] should reduce to $\frac{\rho_s h_s}{\rho_f c \Delta t} < C$ where C is generally on the order of magnitude of unity. In this case we can see that a reasonable order of magnitude for the required time step for an explicit scheme for the model problem is $\Delta t \approx \frac{\rho_s h_s}{\rho_f c} \approx 10^{-7}$ s. Compressibility could allow for an explicit scheme even though this would have been impossible using an incompressible fluid, though in this case the time scales are impractically small. Note that $\frac{\rho_s h_s}{\rho_f \mu_{max}} \approx 10^{-4}$, far below the incompressible range for explicit simulations.

6.7 Transient Divergence

The criterion 5.30 is a necessary criterion for asymptotic convergence, but what if the algorithm takes a detour to get to the converged state? It has been proven that for a compressible, linear fluid-structure interaction problem, the convergence in the fixed point iteration is not monotonous, meaning that even though it converges asymptotically, the norm of the iteration operators $\|\mathcal{J}^n\|$ are not strictly smaller than one. In such cases any error will be amplified, and in the worst case the simulations may crash. [17]

6.8 Incomplete Convergence

The fluid solver runs only 4 inner iterations between each coupling step, and this may make the force field imported into the solid solver irregular, which should have an impact on the displacement field, and may introduce difficulties as the solvers are iterated. Also especially using larger time steps, the coupling algorithm may not be completely converged after a time step, as it often happened in the simulations that a maximum number of inner iterations was reached. This means that the fluid- and solid solvers will take a time step starting from slightly different fields which may negatively impact stability, separate from the added mass effect.

6.9 Effects of Nonlinear Structure

The stiffness matrix $\mathbf{K}$ in the finite element formulation is nonlinear and depends on the configuration. Its eigenvalues will vary with the displacement, and in extreme cases such as buckling these may even turn negative. It is possible that such nonlinear effects contribute to a smaller overall stiffness, which increases the maximal eigenvalue in (5.30). In this case all displacements are relatively small, a fraction of a millimetre, and so the $\mathbf{K}$ matrix will probably remain relatively constant. However, if actual package forming is to be simulated it is unclear how the extreme nonlinearities will impact the structural stiffness and hence the stability. If there are bifurcations in the structural solution, eigenvalues of the $\mathbf{K}$ matrix become negative, which would require ω to be very small or even negative as well, unless the mass matrix is big enough to counteract it in the condition (5.30).

6.10 Time Discretisation Scheme

Apart from giving the errors in the fluid domain a more dispersive nature, the second order time discretisation affects the algorithm stability through the added mass matrix. Using second order time discretisation, equation 5.22 would have a leading term depending on the method of interpolating the velocity of the wall. If using a first order implicit Euler method it would have the form $\mathcal{M}_A \frac{3d^k}{2\Delta t^2}$, in accordance with (3.3), thereby effectively amplifying the added mass effect by $\frac{3}{2}$. If using second order interpolation the added mass effect would be amplified by $\frac{9}{4}$. Therefore it would likely require a lower ω than a 1st order discretisation, depending on the finer details of solver implementation.

6.11 Boundary Conditions

In determining the appropriate eigenfunctions for the pressure for the model problem, it was assumed that the outlet was "open", i.e. connected to an unconfined fluid. Had it been "closed" we would have required $\frac{\partial p}{\partial x} = 0$ at the outlet instead, which would have complicated the analysis as other base functions would have been needed. [13] The outlet is modelled by a *mass flow inlet* in STAR-CCM+, and it is unclear which of the options this corresponds to, if any at all. If these calculations are to be carried out in a setting with a simulated package forming, the conditions would likely correspond to a closed outlet. It is unclear how this may affect the added mass instability.

6.12 Parameter Choices

Simulations have been run using 2nd order time integration, full grid flux and $\beta = 0$. Some parameter sets and their outcomes are available in table 6.1. The last two worked well until suction 1 where possibly nonlinear effects caused a crash. The surface average incremental displacement and a picture of the cross section of the crash for the uncertain case with $\Delta t = 2$ ms from table 6.1 are available in figure 6.10. It is possible that smaller ω or even larger Δt may be needed when using $\beta = 0$ and second order time integration. Another possibility is that there are destabilising effects of increasing Δt due to viscosity or other phenomena that have not been explored in this thesis.

Δt (ms)	ω	Result	Verdict
1	0.15	Unstable after 0.24 t_{sim}	Unstable
2	0.25	Unstable after 0.23 t_{sim}	Unstable
2	0.12	Hit wall at suction 1	Uncertain
4	0.15	Hit wall at suction 1	Uncertain

Table 6.1: Some parameter sets using $\beta = 0$, full grid flux and 2nd order time integration.

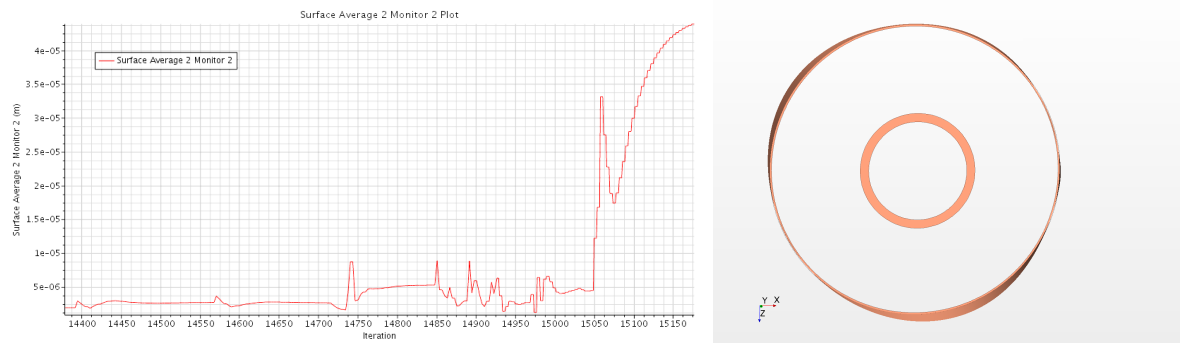

Figure 6.10: The surface average displacement (left) and flange cross-section during the crash for a case using $\Delta t = 2$ ms, $\omega = 0.12$, grid flux 1 and 2nd order time integration.

In order to avoid collision with the pressure flange several different damping coefficients μ_0 have been tested. The damping coefficient is hard to estimate, but the Abaqus manual suggests setting it to $\mu_o = F/v$ where F is an estimated force between the surfaces, and v is an estimated impact speed. v was estimated to be around 10^{-2} m/s, but the contact force is hard to measure. Therefore it was set to 1 N, giving $\mu_0 = 100$ kg/s. This caused the algorithm to crash, but it is unclear if it was due to physical contact or numerical difficulties associated with high gradients introduced by the contact formulation. Subsequently $\mu_0 = 10^5$ kg/s was tested and it failed in a similar way. This leads to the suspicion that both are too large. The two last cases using second order time integration, $\beta = 0$ and full grid flux in table 6.1 used $\mu_0 = 1$ kg/s for the 4 ms case and 10 kg/s for the 2 ms case, both without success as the wall hit the pressure flange. Maybe the clearance distance should be increased or another contact formulation could be considered, or maybe the time steps were too large for the contact damping to work efficiently. For both cases marked *Uncertain* in table 6.1 it is likely that the solution lost stability due to nonlinear effects, and the contact damping made the displacement monitor at the crash look like it was slowly converging. The Abaqus output file indicated that the contact condition was active at the time of the crash.

Chapter 7

Conclusions

The cause of instabilities in the FSI coupling algorithm is primarily due to the added mass effect. In order to make a simulation converge it is possible to decrease the under-relaxation factor ω, but in some cases depending on the geometry and material parameters of the problem, this may be required to be very low. Similarly the time step can be increased, but at the cost of numerical dissipation and increased discretisation errors. However, as can be seen in figures 6.1-6.8, for many geometries and cases the condition on ω are very reasonable. It seems that as a rule of thumb partitioned implicit FSI problems can be stabilised by setting ω low enough, a valuable insight for the future.

The relation between ω and the time step Δt is counter-intuitive as smaller time steps has a negative effect on stability, counter to the usual reflex of decreasing the time step in order to keep a simulation stable. Thus there is a weigh-off between using small time steps for physical accuracy and large ones for stability and computational efficiency. There are of course other phenomena that limit the time step, but the conditions on ω above can help with selecting a suitable Δt for different applications.

Using β damping to keep the algorithm stable is effective as the criterion on ω gets much less severe, but the solution is damped out substantially. Therefore β should be decreased or even set to 0. The main effect of β on stability is on the smaller time steps, see figure 6.7, so using a larger time step rather than trying to compensate with ω may be a good idea when setting β low.

The grid flux under-relaxation is similar in that it seems to permit running with higher ω but changes the solution. Unlike β the solution does not seem to be monotonously damped out by setting the grid flux URF lower and the changes can be unpredictable. It is recommended not to use grid flux under-relaxation at all.

The time discretisation order in the fluid solver affects the solution as well, but will likely cause a worse added mass effect. The most suitable time discretisation order probably varies from application to application, and has to be weighed against increasing Δt or decreasing ω.

The tube application was investigated analytically with respect to stability and a criteria on ω was found depending on the tube length, radius, wall thickness, densities, Young's modulus and β. It seems the correspondence to the numerical application is good, and can indicate the onset of instability and the effect of changes of parameters. Increasing length, radius, fluid density, decreasing wall thickness, β and Young's modulus will all negatively affect stability and require lower ω or larger Δt.

Chapter 8

Limitations and Suggestions for Future Work

The effect of incompressibility hasn't been investigated in this thesis. Since the theoretical derivation of the stability criteria on ω assumes incompressible flow it would be very interesting to study if compressibility has any effect on the algorithm stability. It would also be interesting to investigate its effect on the solution.

Attempts were made to implement contact damping but no working parameter set has been found. Either the parameters could be investigated further and fine tuned to values that work in some cases or another contact formulation could be considered.

Further attempts to use $\beta = 0$, grid flux 1 and 2nd order time integration should be made. A good starting point is the criterion on ω and Δt imposed by the model problem for $\beta = 0$ in figure 6.7. The free surface will lessen the added mass effect but second order time integration will make it worse.

The probe points 2 and 3, seen in figure 4.1, may not be suitable to represent the dynamical behaviour of the system. No probe was placed right between the outlet and the pressure flange where perhaps the most interesting behaviour takes place, and the tangential placement of probe 3 turned out to be close to a node for the mode $n = 3$ which likely won't show the full range of displacement behaviour during suction.

Experience indicates that grid flux under-relaxation helps the solution converge, but it is unclear how this enters into the stability criterion.

The anisotropic material in the tube was not accounted for in the stability criterion.

Other convergence criteria should be explored, in particular to make sure the fluid velocity field is converged in each time step.

The number of inner iterations in STAR-CCM+ between FSI couplings has been set to 4 throughout this thesis. The theoretical stability analysis assumes a fully converged flow field at each coupling step and it not known how this discrepancy affects stability. Sometimes using larger time steps the coupling between the fluid- and structural solvers may not be fully converged. this introduces error which may have an impact on stability, and these effects should be investigated.

The model used in this thesis was reduced in order to save computational time, and it is possible that the mesh didn't resolve the domain sufficiently well. Especially the delicate dynamics around the pressure flange might have changed if the mesh was refined in this area, and maybe it would even solve the problem of the wall hitting the flange. In the future a mesh study could be performed.

Partitioned schemes using algorithm 1 are subject to added mass instability, but there are other possibilities. For example a monolithic solution method could solve the stability problem, but is difficult to implement. Another possibility is for the fluid- and structural solvers to communicate more and implement more efficient and stable coupling schemes. See [18] for examples of schemes that could be implemented by the software manufacturers.

One stated goal is to simulate the whole package forming process, which might require an explicit time integration method on the solid side. These numerical schemes have not been studied in this thesis, and it is unclear if it is possible to couple an explicitly advancing Abaqus case with an implicit FSI algorithm, or if it is at all possible to use an explicit FSI coupling. The effects on stability of heavily non-linear structural behaviour during package forming remains unclear. The numerical calculation method proposed in chapter 5.6 could be implemented to investigate if and how structural non-linearity affects the stability. The possibility to run LES simulations for better accuracy should be considered, and the numerics of this case investigated.

Bibliography

[1] O.C. Zienkiewicz, R.L. Taylor, and J.Z. Zhu. 18 - coupled systems. In O.C. Zienkiewicz, R.L. Taylor, and J.Z. Zhu, editors, *The Finite Element Method Set*, pages 631 – 663. Butterworth-Heinemann, Oxford, sixth edition, 2005.

[2] A.H. Techet. Added mass - 2.016 hydrodynamics, 2005. `http://ocw.mit.edu/courses/mechanical-engineering/2-016-hydrodynamics-13-012-fall-2005/readings/2005reading6.pdf`. Accessed June 9, 2016.

[3] Miguel A Fernández and Jean-Frédéric Gerbeau. Algorithms for fluid-structure interaction problems. In *Cardiovascular mathematics*, pages 307–346. Springer, 2009.

[4] CD-adapco. *Star-CCM+ 10.06.009 User Guide*.

[5] Matti Ristinmaa. *Introduction to the Non-Linear Finite Element Method*. Division of Solid Mechanics, Lund University, 2008.

[6] Daniel HIMR, Vladimír HABAN, and F Pochly. Sound speed in the fluid-gas mixture. In *3rd IAHR International meeting of the Workshop on Cavitation and Dynamic Problems in Hydraulic Machinery and Systems, Brno, Czech Republic*, pages 14–16, 2009.

[7] Arris S Tijsseling and Alexander Anderson. The joukowsky equation for fluids and solids. In *Proceedings of the 9th International Conference on Pressure Surges*, pages 739–751, 2004.

[8] Dassault Systèmes. *Abaqus 6.14 Documentation*.

[9] P. Causin, J.F. Gerbeau, and F. Nobile. Added-mass effect in the design of partitioned algorithms for fluid–structure problems. *Computer Methods in Applied Mechanics and Engineering*, 194(42–44):4506 – 4527, 2005.

[10] Christiane Förster, Wolfgang A Wall, and Ekkehard Ramm. The artificial added mass effect in sequential staggered fluid-structure interaction algorithms. In *ECCOMAS CFD 2006: Proceedings of the European Conference on Computational Fluid Dynamics, Egmond aan Zee, The Netherlands, September 5-8, 2006*. Delft University of Technology; European Community on Computational Methods in Applied Sciences (ECCOMAS), 2006.

[11] Sherman C. P. Cheung Kelvin K. L. Wong, Pongpat Thavornpattanapong and Jiyuan Tu. Numerical stability of partitioned approach in fluid-structure interaction for a deformable thin-walled vessel. *Computational and Mathematical Methods in Medicine*, 2013, 2013.

[12] François Axisa and Philippe Trompette. Chapter 8 - bent and twisted arches and shells. In François Axisa and Philippe Trompette, editors, *Structural Elements*, volume 2 of *Modelling of Mechanical Systems*, pages 391 – 440. Butterworth-Heinemann, 2005.

[13] Michael P. Paidoussis. Chapter 7 - cylindrical shells containing or immersed in flow: Basic dynamics. In Michael P. Paidoussis, editor, *Fluid-Structure Interactions (Second Edition)*, pages 551 – 713. Academic Press, Oxford, second edition edition, 2014.

[14] Silvano Erlicher, Luca Bonaventura, and Oreste S Bursi. The analysis of the generalized-α method for non-linear dynamic problems. *Computational Mechanics*, 28(2):83–104, 2002.

[15] Michael P. Paidoussis. Chapter 2 - concepts, definitions and methods in fluid-structure interactions. In Michael P. Paidoussis, editor, *Fluid-Structure Interactions (Second Edition)*, pages 7 – 62. Academic Press, Oxford, second edition edition, 2014.

[16] EH Van Brummelen. Added mass effects of compressible and incompressible flows in fluid-structure interaction. *Journal of Applied mechanics*, 76(2):021206, 2009.

[17] EH Van Brummelen and René de Borst. On the nonnormality of subiteration for a fluid-structure-interaction problem. *SIAM Journal on Scientific Computing*, 27(2):599–621, 2005.

[18] Joris Degroote. Partitioned simulation of fluid-structure interaction. *Archives of Computational Methods in Engineering*, 20(3):185–238, 2013.